Supplement of Geochronology, 8, 223–253, 2026
https://doi.org/10.5194/gchron-8-223-2026-supplement

Supplement of

Dating Late Pleistocene pluvial lake shorelines in the Great Basin, USA using rock surface luminescence dating techniques: developing new approaches for challenging lithologies

Christina M. Neudorf et al.

Correspondence to: Christina M. Neudorf (c.neudorf@vicus.net.au)

Supplementary Material

S1. Study sites

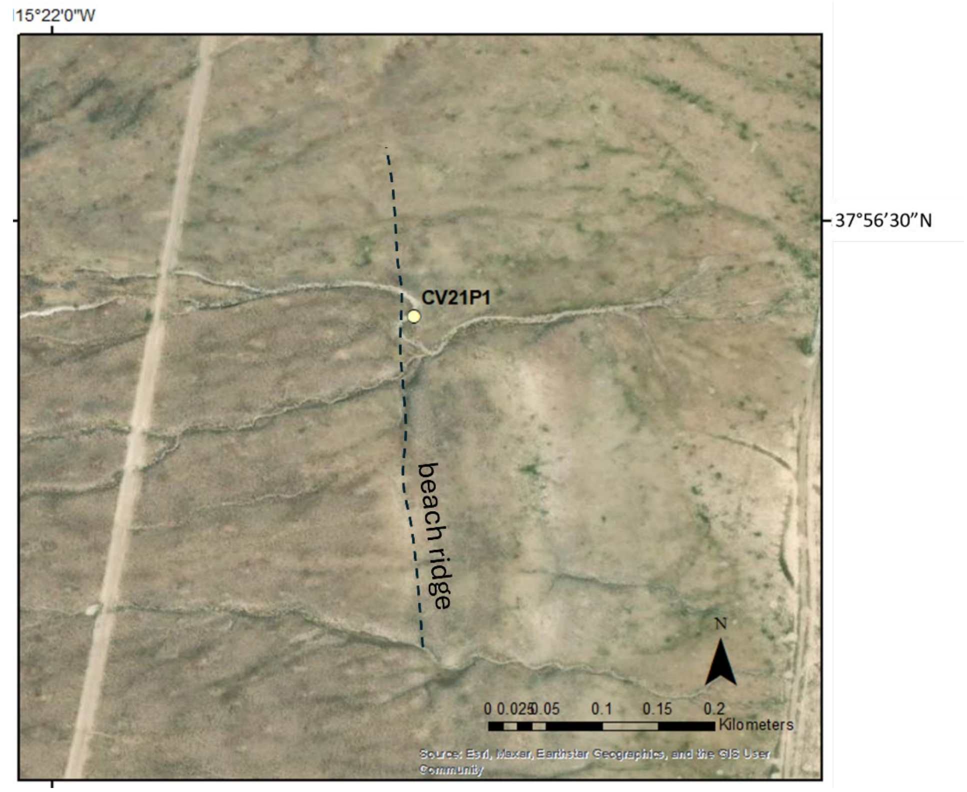

Figure S1. The location of study site CV21P1 on the highest shoreline feature in western Coal Valley. Basemap: ESRI, Maxar, Earthstar Geographics, and the GIS User Community | Powered by Esri.

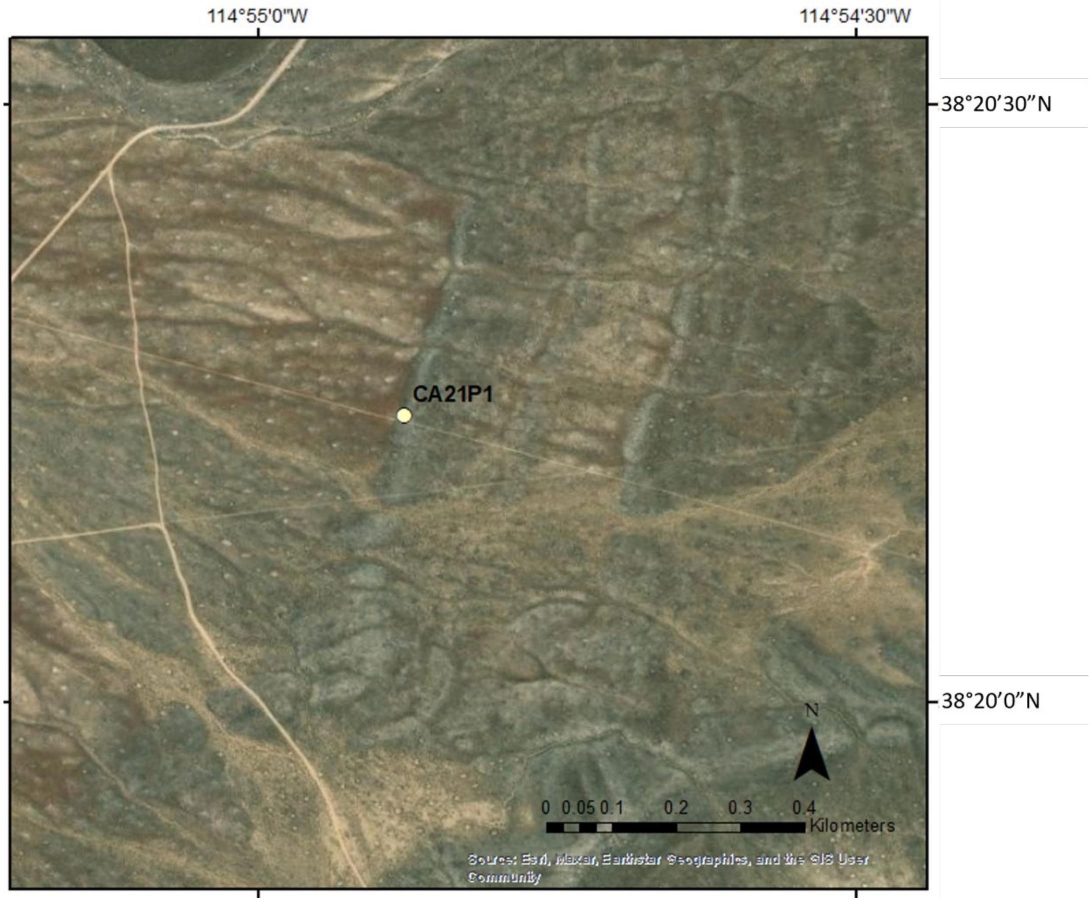

Figure S2. The location of study site CA21P1 on the highest shoreline feature in western Cave Valley. Basemap: ESRI, Maxar, Earthstar Geographics, and the GIS User Community | Powered by Esri.

Figure S3. The location of CA21P2 on a high shoreline feature in southwestern Cave Valley. Basemap: ESRI, Maxar, Earthstar Geographics, and the GIS User Community | Powered by Esri.

Figure S4. The location of study site LK21P1 on the highest shoreline feature in western Lake Valley. Basemap: ESRI, Maxar, Earthstar Geographics, and the GIS User Community | Powered by Esri.

Table S1. Independent age control for Coal, Cave and Lake valleys.

Lab #	Lake basin	Feature	Material	Method	Age[1]	Cal yrs BP median probability[2]	Cal yrs BP 2-sigma range[2]	Reference
D-AMS 029792	Coal Valley	Highstand lake shoreline	Lymnaeidae Stagnicola sp. shell	Radiocarbon	13,366 ± 59 yrs BP	16,088	15,873-16,281	Wriston and Adams, 2020
USU-2527	Cave Valley	Low-level lake sediments	Quartz	Luminescence (multi-grain aliquot)	11.33 ± 1.68 ka			Duke and Young, 2018
Beta-440300	Cave Valley	Soil	Organic sediment	Radiocarbon	8,380 ± 30 yrs BP	9,422	9,299-9,383 & 9,397-9,481	Duke and Young, 2018
Beta-50773	Lake Valley	Highstand lake shoreline	Unreported	Radiocarbon	14,210 ± 100 yrs BP	17,258	17,011-17,536 & 17,629-17,699	Currey in Lillquist, 1994
D-AMS 20244	Lake Valley	Wetland sediments	Organic sediment	Radiocarbon	10,656 ± 48 yrs BP	12,685	12,505-12,526 & 12,614-12,735	Duke and Young, 2018
USU-2529	Lake Valley	Inset lake shoreline	Quartz	Luminescence (multi-grain aliquot)	9.27 ± 1.87 ka			Duke & Young, 2018

[1] Radiocarbon ages are reported in years before present (yrs BP) and are not calibrated. Luminescence ages are reported in kilo annum (ka).

[2] Radiocarbon years are calibrated with IntCal 20.14c using Calib 8.2 (Reimer et al., 2020). The two radiocarbon age ranges reported for samples Beta-50773 and D-AMS 20244 reflect two age interceptions onto the IntCal20 calibration curve.

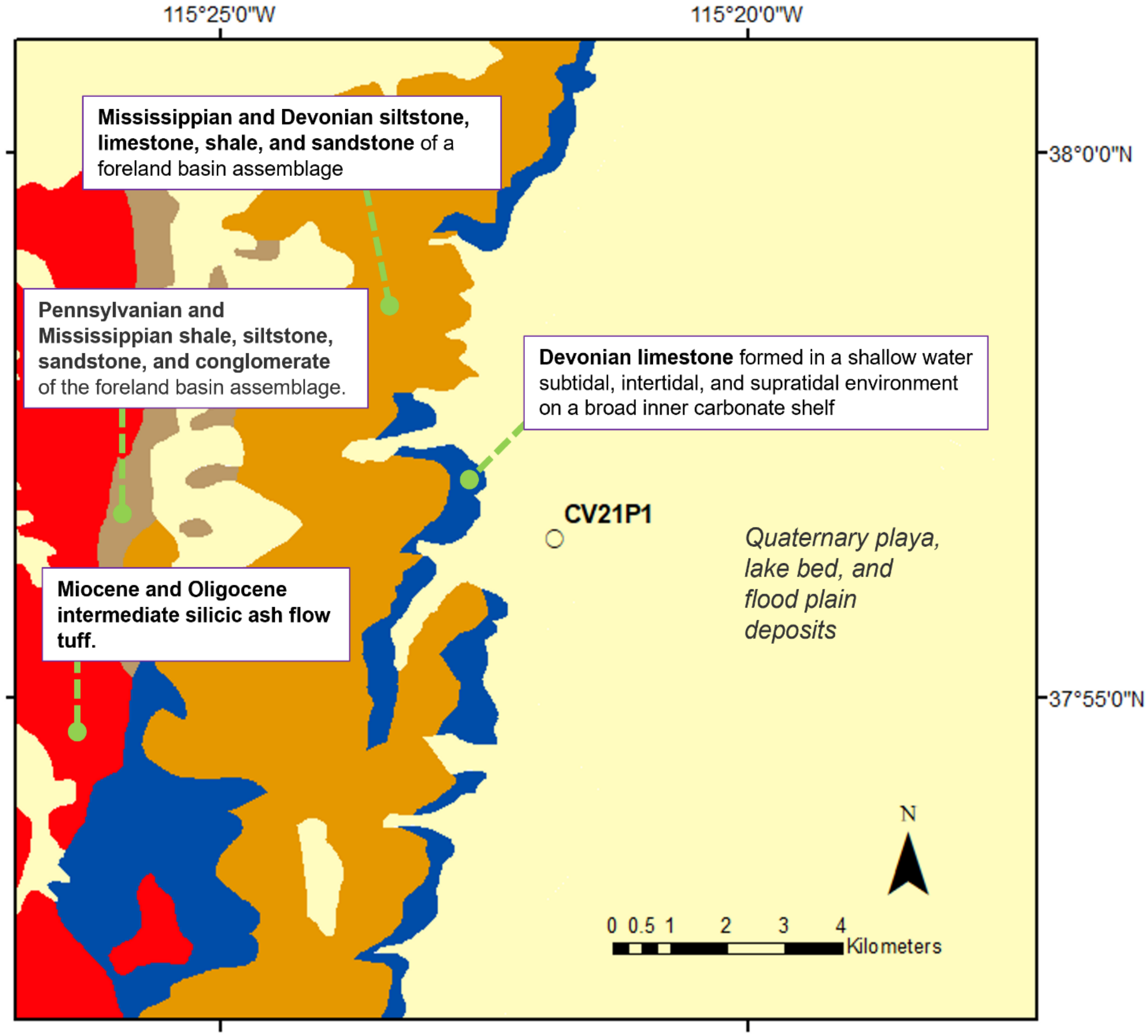

Figure S5. Site CV21P1 is located east of the Guilmette Formation (Devonian limestone) and the Joana, Mercury and Bristol Pass Limestones (Mississippian and Devonian foreland basin assemblage). Generalized surficial geology after Crafford (2007), scale 1:250,000.

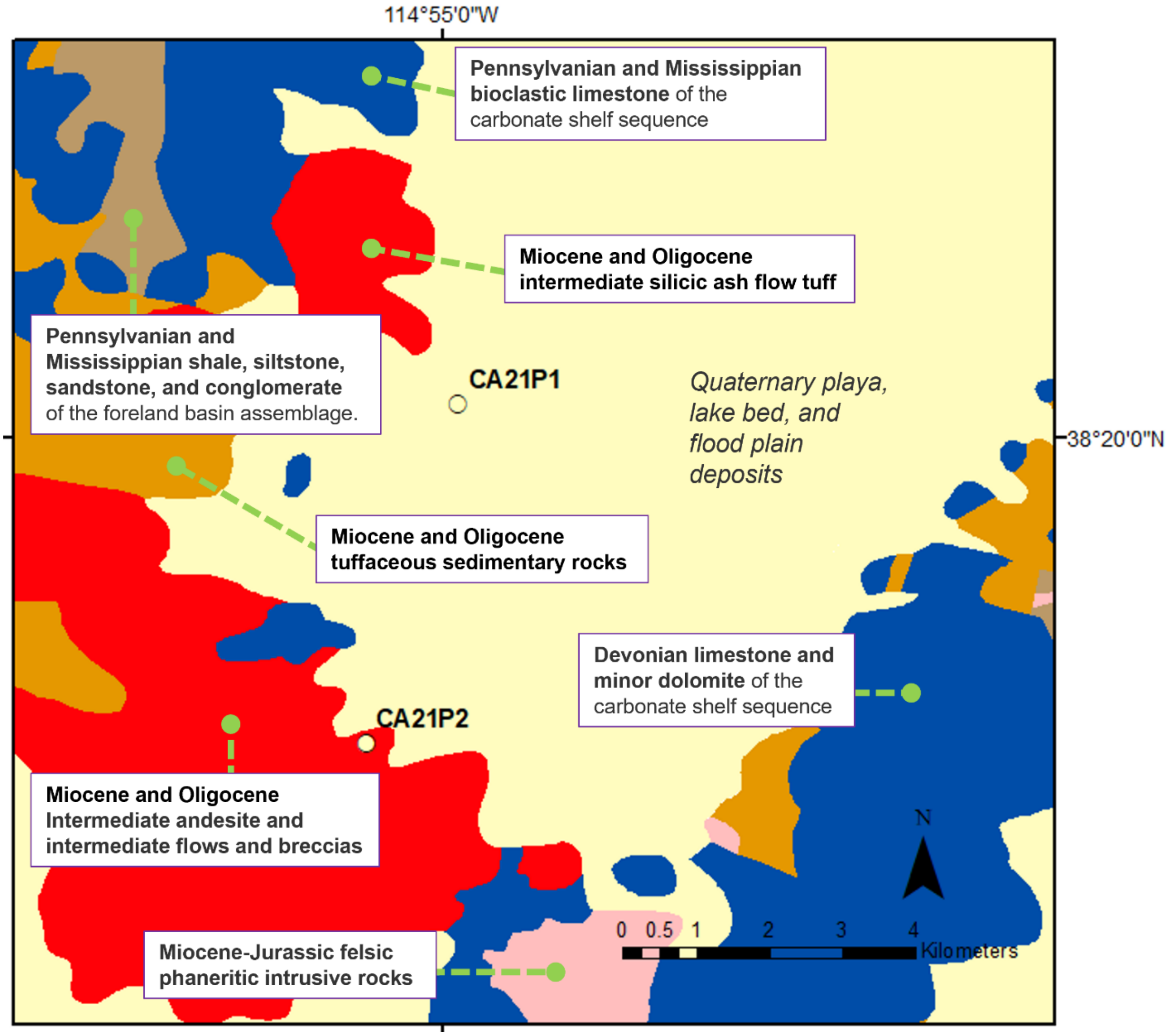

Figure S6. Sites CA21P1 and CA21P2 east of undifferentiated older volcanics with pockets of Pennsylvanian limestone as well as Scotty's Wash quartzite and Chainman shale of upper Mississippian age in the Egan Range. Generalized surficial geology after Crafford (2007), scale 1:250,000.

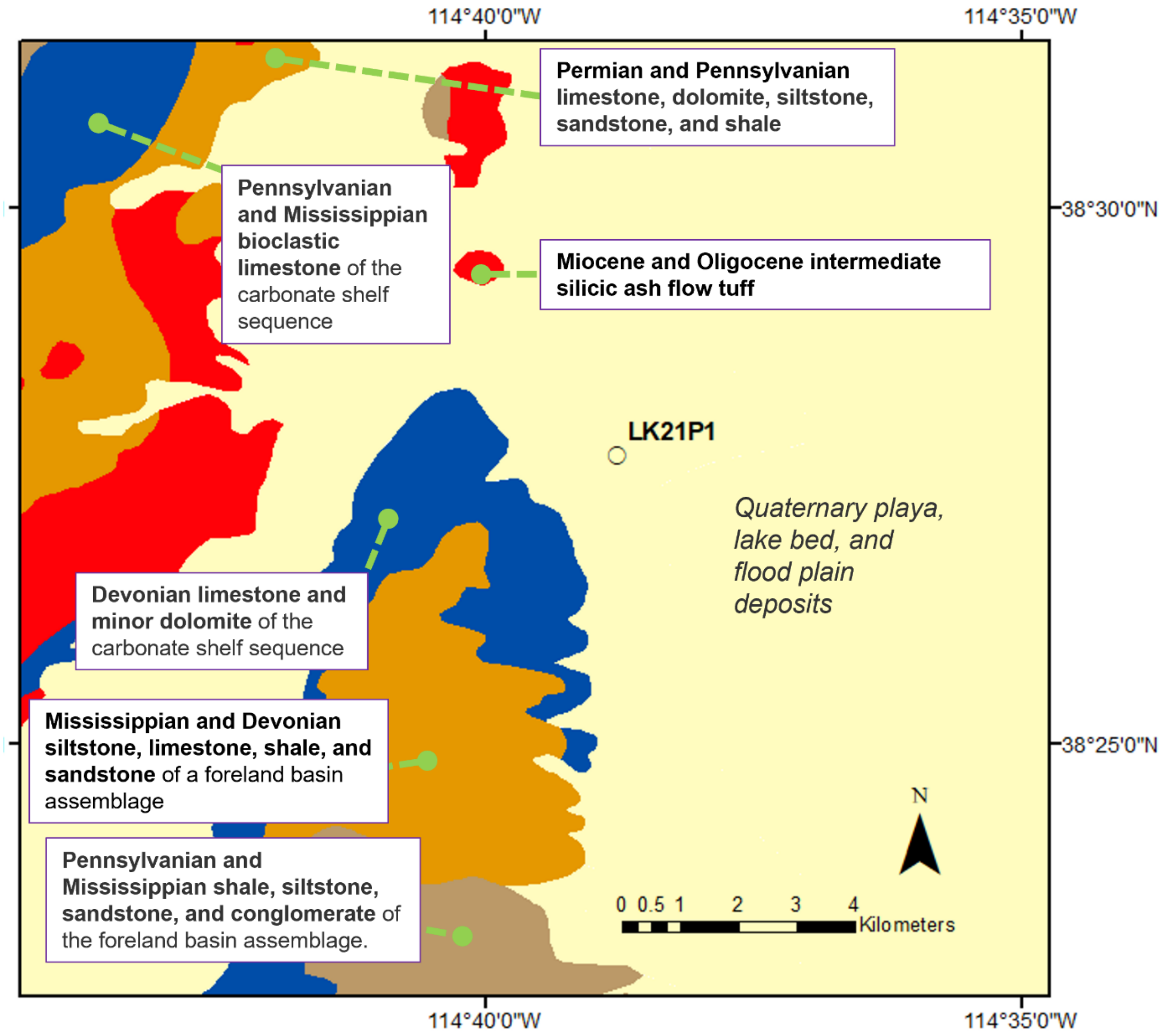

Figure S7. Site LK21P1 located east of middle to upper Devonian Guilmette formation Dolomite and Devils Gate Limestones. Generalized surficial geology from Crafford (2007), scale 1:250,000.

S2. SAR protocols tested on volcanic rocks

Table S2. Lower-temperature (180°C & 225°C) pIRIR protocols tested in this study.

Step	$pIRIR_{180}$ (multi-grain)	$pIRIR_{225}$ (multi-grain)
1	Natural/Regenerative Dose	Natural/Regenerative Dose
2	Preheat (200°C, 10 s)	Preheat (250°C, 10 s)
3	IR diodes (50°C, 100 s)	IR diodes (50°C, 100 s)
4	IR diodes (180°C, 100 s) → L_n, L_x	IR diodes (225°C, 100 s) → L_n, L_x
5	Test dose (~10 Gy)	Test dose (~10 Gy)
6	Preheat (200°C, 10 s)	Preheat (250°C, 10 s)
7	IR diodes (50°C, 100 s)	IR diodes (50°C, 100 s)
8	IR diodes (180°C, 100 s) → T_n, T_x	IR diodes (225°C, 100 s) → T_n, T_x
9	IR diodes (200°C, 40 s)	IR diodes (290°C, 40 s)
10	Return to step 1.	Return to step 1.

S3. CW- and LM-OSL measurements

S3.1 Continuous wave measurements

Standard D_e measurement from quartz extracts typically involves continuous wave (CW) light stimulation at 125℃ and luminescence detection using UV filters with emissions centered at 365 nm. If contamination from feldspar is anticipated, such as we expect in our polymineral samples, blue light stimulation is often preceded by stimulation with infrared (IR) diodes to bleach any signal contribution from feldspar without further bleaching the signal from quartz (also known as a post-IR OSL measurement, Roberts, 2007). For sediment extracts from samples in this study, both the OSL (here meaning optically stimulated luminescence detected during blue light stimulation) and the post-IR OSL were measured to determine if there is a signal from quartz that can be isolated from feldspar signal contamination using an IR bleach (Tables S3-S5). Samples with signals coming mainly from quartz were expected to have OSL and the post-IR OSL signals of similar intensity implying negligible signal reduction due to IR bleaching of feldspar. Samples with signals coming mainly, or in part, from contaminating feldspar were expected to have post-IR OSL signals that are less intense than the OSL signals, as well as a prominent IR signal. In some samples, neither the IR signal from feldspar, nor the OSL signal from quartz yielded a detectable signal.

Coal Valley CW signals

Most Coal Valley samples measured from limestone rocks exhibited OSL signals that were drastically reduced after IR stimulation (e.g., Rock 11, Table S3). Thus, we concluded that quartz minerals within the limestones are not reliable for dating and further testing should focus on the IR signals from feldspar. Some limestone gravels collected from site CV21P1 yielded minerals with a clear IR signal with photon counts of 800 counts/second or more (e.g., Rock 11, Table S3).

Cave Valley CW signals

In the case of the volcanic rocks from Cave Valley, OSL and post-IR OSL signals were often similar in intensity, though many rocks did not have a detectable IRSL signal (e.g., Rock 1, Table S4). Out of 20 rocks tested, 7 exhibited a detectable IRSL signal and photos of these rocks after sample preparation are shown in Supplementary Material Section 4 below. Volcanic rocks with the brightest signals (typically with bright IR signals, e.g., Rock 4, Table S4) were typically of the felsic (andesitic or rhyolitic) varieties, whereas basalts, like those collected from site CA21P2, had no signal (Table S5).

S3.2 LM-OSL measurements

LM-OSL curves (Bulur, 1996) were measured from a subset of limestone and volcanic gravel sediment extracts (Tables S3-S5). Each LM-OSL signal was measured with blue LEDs where the stimulation power was ramped from 0 to 90% over 3600 s and each LM-OSL measurement was preceded by an IR stimulation at 50°C to deplete any signal from contaminating feldspars. No fast component was detected from quartz in any of the polymineral samples obtained from limestone or volcanic rocks, suggesting that further testing should focus on the IR signal from feldspar in both rock lithologies.

Table S3. OSL, IRSL, post-IR OSL and LM-OSL signals for limestone sediment extracts from Rocks 11 and 14 from Coal Valley site CV21P1. The UV filter is used to detect 365 nm wavelength luminescence emissions from quartz (or contaminating feldspar using IR stimulation), while the violet filter detects 410 nm wavelength emissions from feldspar.

Rock sample	Detection filter		
	UV filter (U-340)	Violet filter (Schott BG-3 & BG39)	UV filter (U-340)
Rock 11	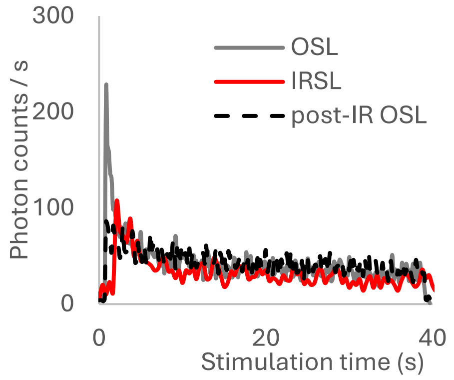	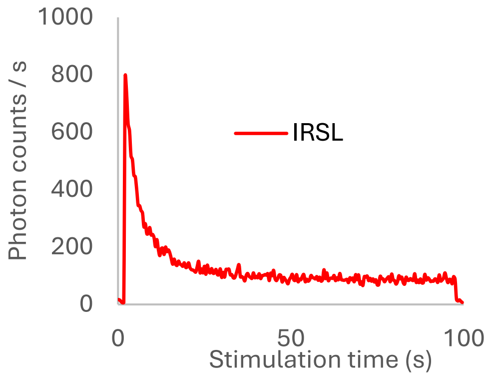	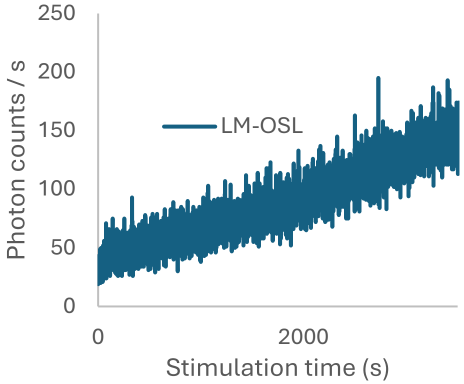
Rock 14	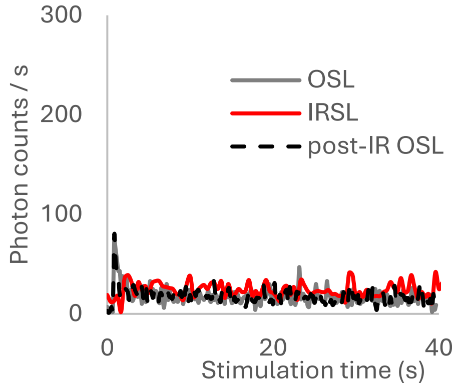	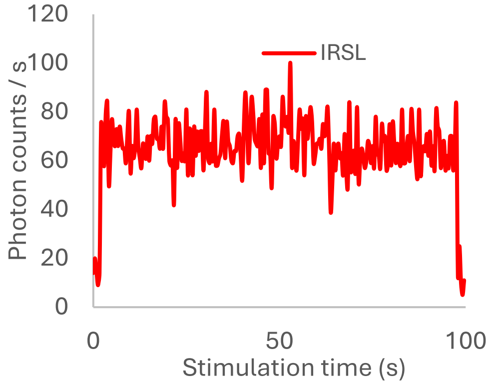	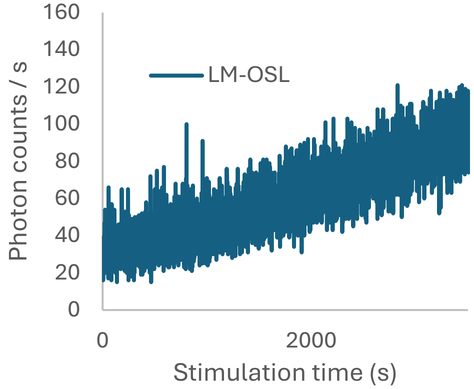

Table S4. OSL, IRSL, post-IR OSL and LM-OSL signals for Rocks 1 and 4 from Cave Valley site CA21P1. The UV filter is used to detect 365 nm wavelength luminescence emissions from quartz (or contaminating feldspar using IR stimulation), while the violet filter detects 410 nm wavelength emissions from feldspar.

Rock sample	Detection filters		
	UV filter (U-340)	Violet filter (Schott BG-3 & BG39)	UV filter (U-340)
Rock 1	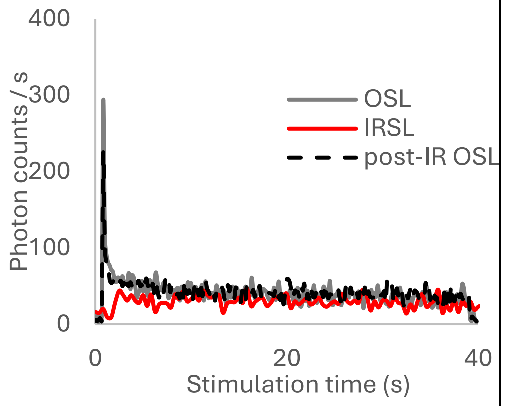	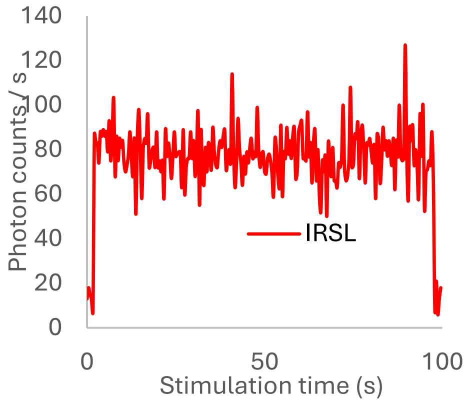	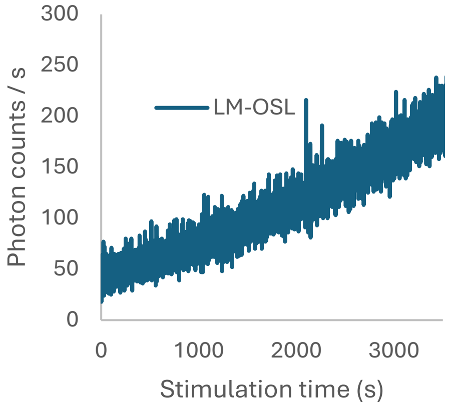
Rock 4	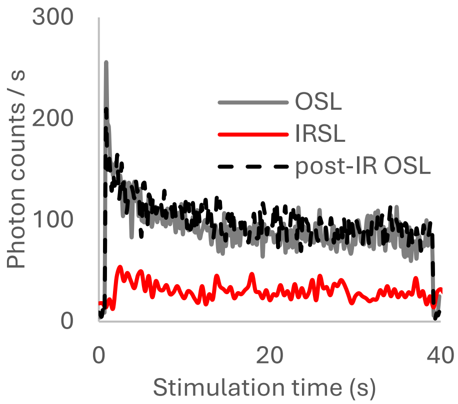	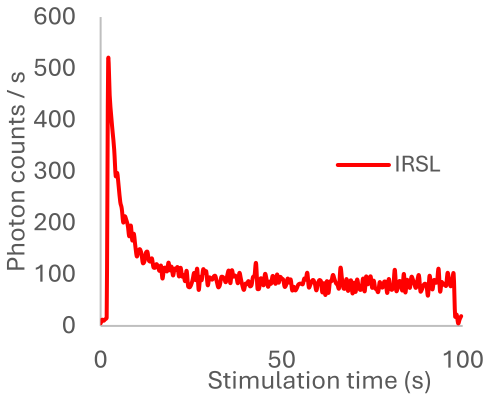	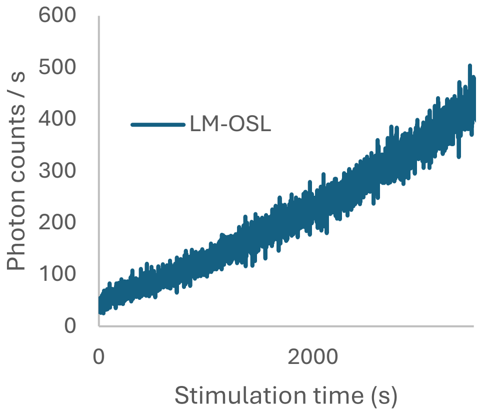

Table S5. OSL, IRSL, post-IR OSL and LM-OSL signals for 2 volcanic rocks from Cave Valley site CA21P2. The UV filter is used to detect 365 nm wavelength luminescence emissions from quartz (or contaminating feldspar using IR stimulation), while the violet filter detects 410 nm wavelength emissions from feldspar.

Rock Sample	Detection filters		
	UV filter (U-340)	Violet filter (Schott BG-3 & BG39) (IR$_{50}$)	UV filter (U-340) (LM-OSL)
Rock 1	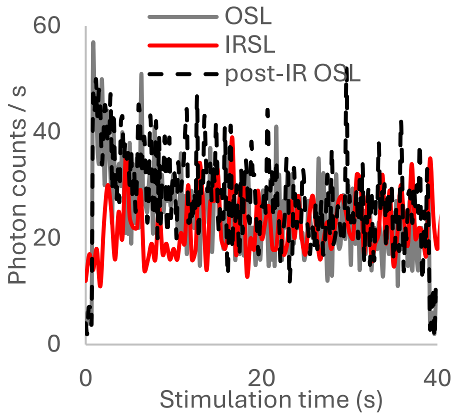	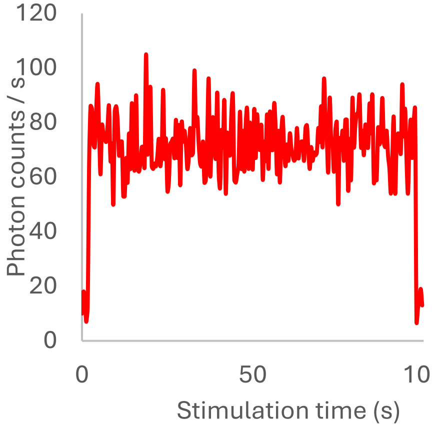	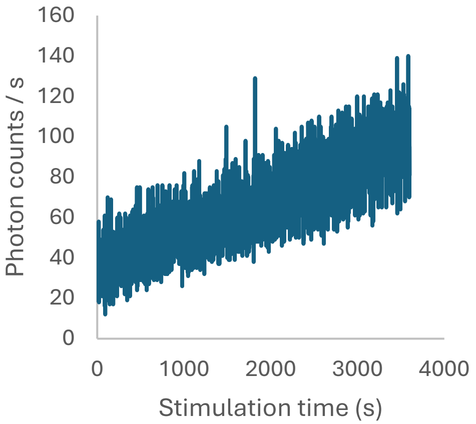
Rock 2	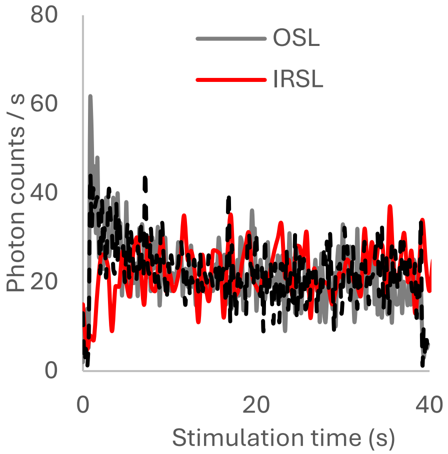	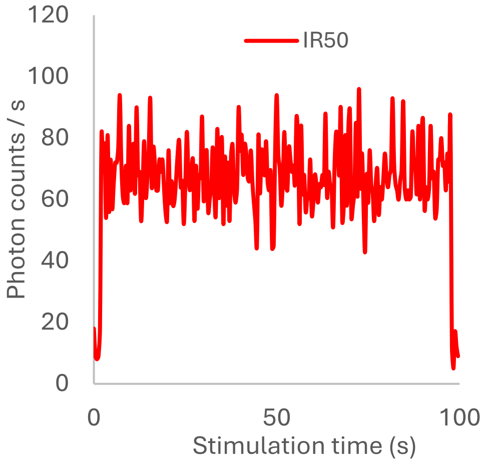	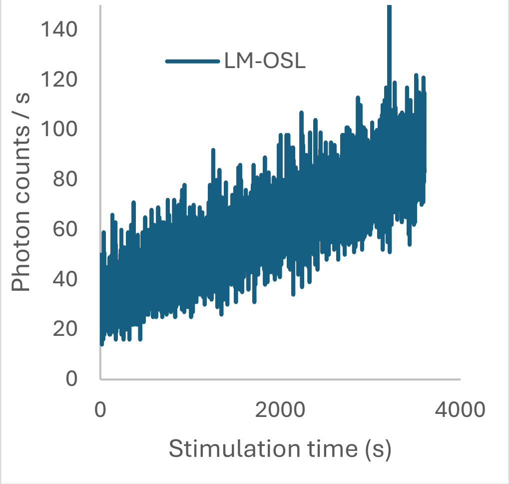

S4. Cored volcanic rocks from site CA21P1, Cave Valley

A) Rock 4

B) Rock 7

C) Rock 11

D) Rock 12

E) Rock 13

F) Rock 14

G) Rock 18

Figure S8. Rocks sampled for signal testing and dating from site CA21P1. Photos have been taken after core extraction and dremeling of the surface. Rock 14 was found to be dominated by chert (cryptocrystalline quartz) and was not dated.

S5. Dose recovery test results

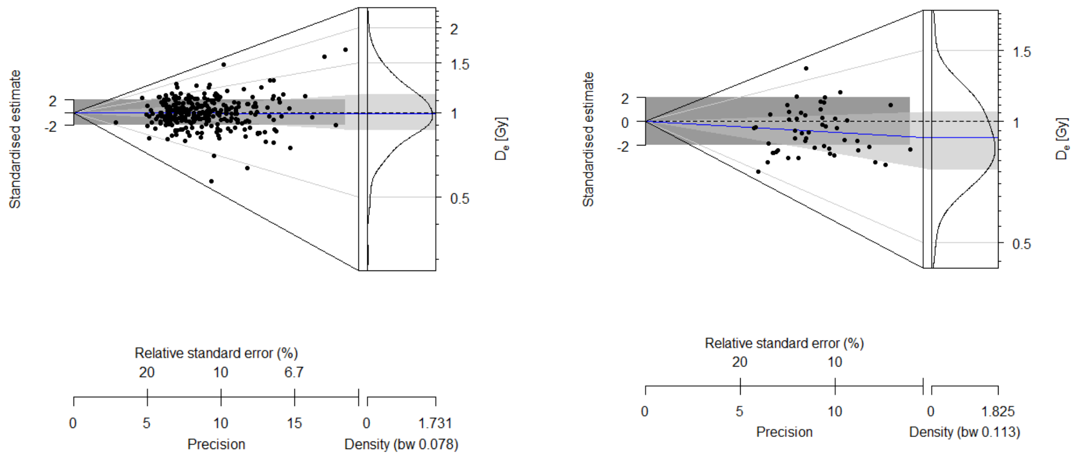
A) Rock 2 (63-90 µm fraction), n=285

B) Rock 10 (125-180 µm fraction), n=50

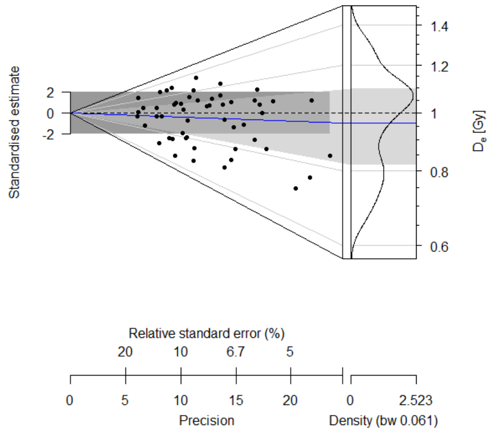
C) Rock 18 (180-250 µm fraction), n=53

Figure S9. Dose recovery test results for polyminerals extracted from limestone clasts of CV21P1. Abanico plots were generated using the “Luminescence” R package (Dietze, 2021; Dietze and Kreutzer, 2021).

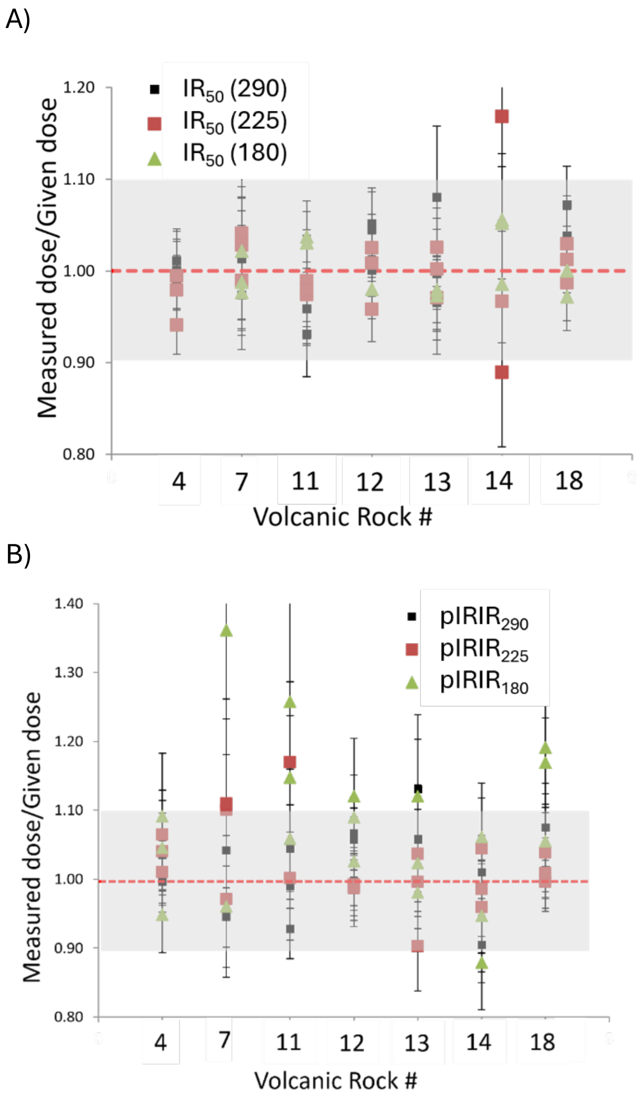

Figure S10. Dose recovery test results for volcanic rocks collected from site CA21P1 in Cave Valley using IR_{50} signals (A) and pIRIR signals (B). Each dot represents one 3 mm diameter multi-grain aliquot. Measured/given dose ratios that fall within 10% of unity (grey shading) are considered favorable and evidence that the SAR protocol is suitable for the sample.

A) Rock 4->sigma-b = 0% (IR_{50}), 0% ($pIRIR_{290}$)

B) Rock 7->sigma-b = 2% (IR_{50}), 0% ($pIRIR_{290}$)

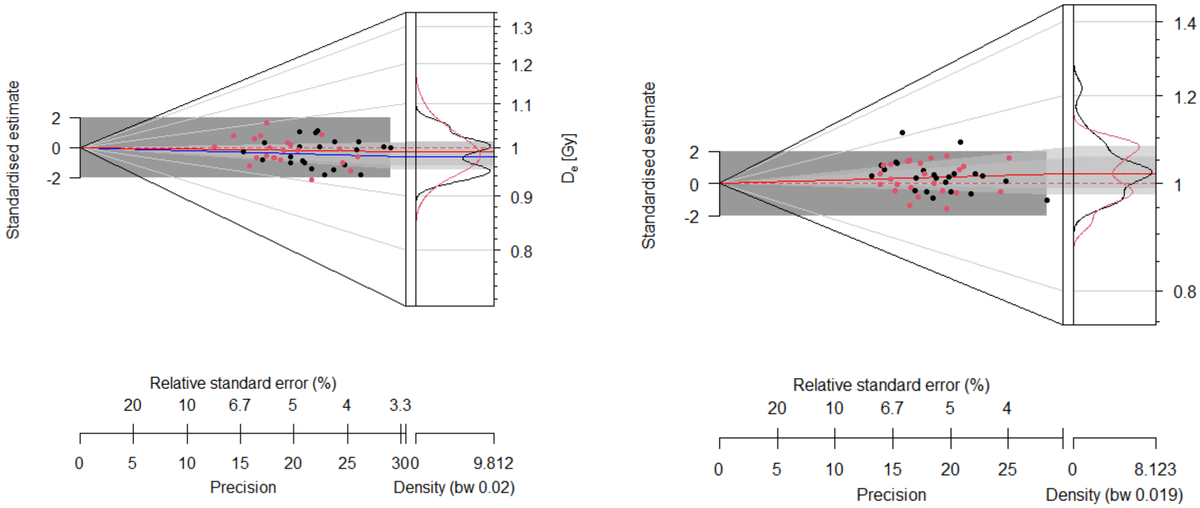

C) Rock 11->sigma-b = 0% (IR_{50}), 5% ($pIRIR_{290}$)

D) Rock 12->sigma-b = 3% (IR_{50}), 0% ($pIRIR_{290}$)

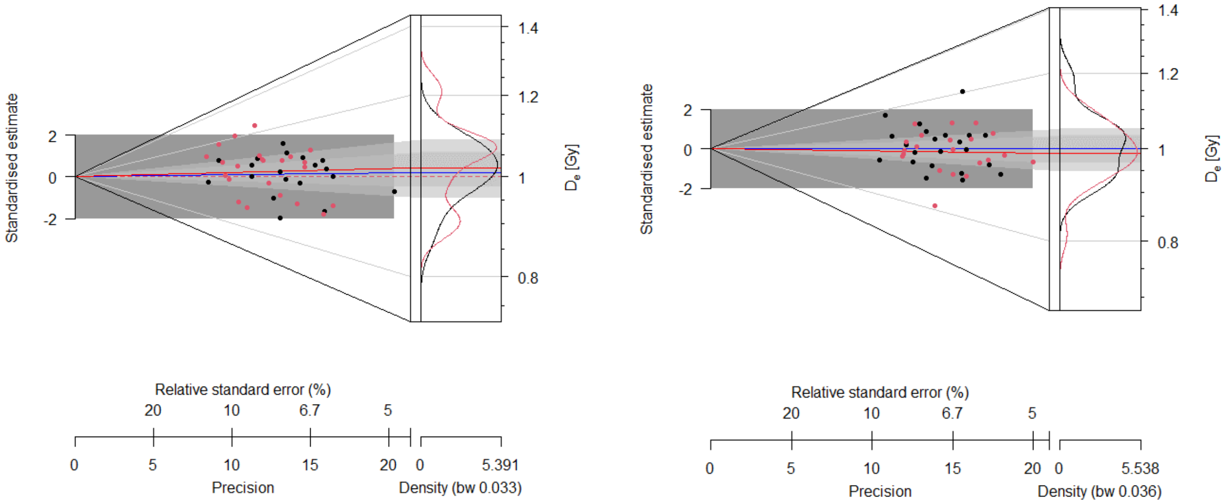

E) Rock 13 ->sigma-b = 5% (IR_{50}), 3% ($pIRIR_{290}$)

F) Rock 18 ->sigma-b = 12% (IR_{50}), 6% ($pIRIR_{290}$)

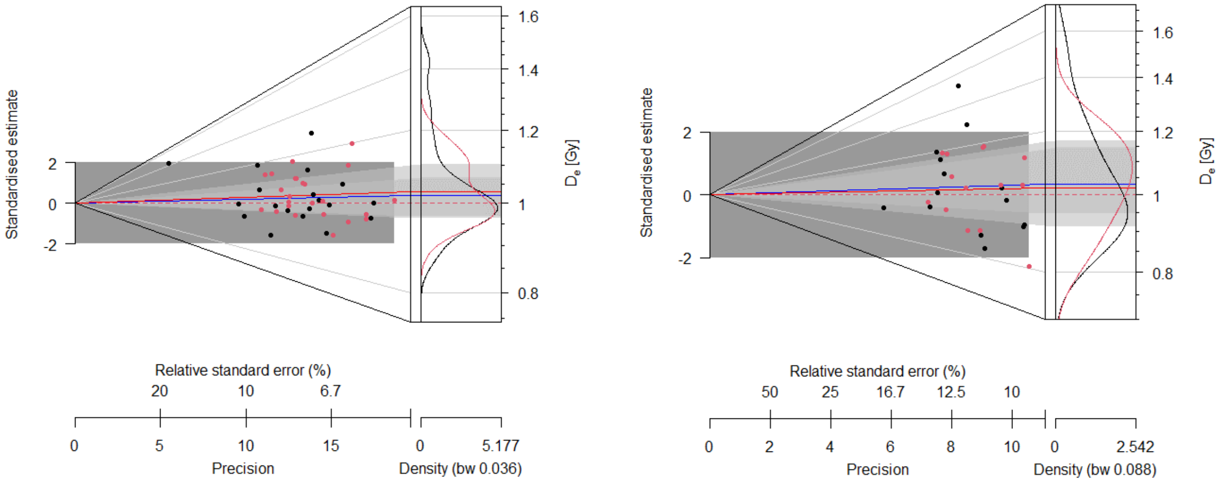

Figure S11. Dose recovery test results for the ground and suspension settled 32-63 µm fraction of volcanic rocks 4, 7, 11, 12, 13, 18 from CA21P1 in Cave Valley. A minimum of 24 multi-grain aliquots were measured and results include aliquots that passed SAR aliquot rejection criteria. Black dots are measured/given dose ratio values for the IR_{50} signal, and red dots are those for the $pIRIR_{290}$ signal. Abanico plots were generated using the “Luminescence” R package (Dietze, 2021; Dietze and Kreutzer, 2021).

Table S6. Dose recovery test results for volcanic rocks used for dating at site CA21P1 in Cave Valley. The IR$_{50}$ signal measured from the 32-63 µm fractions was measured using the IR$_{50}$ SAR protocol with a 160 °C preheat (Table 2). Measured/given ratios are also given for the IR$_{50}$ signals measured during each of the three pIRIR protocols for the 180-250 µm grain size fraction and these are referred to as IR$_{50}$ (PIRIR$_{xxx}$) signals. n = number of accepted aliquots/number of measured aliquots.

Rock sample	Grain size (µm)	Signal	Measured/given dose ratio	Sigma-b (%)
Rock 4	32-63	IR$_{50}$	0.98 ± 0.01 (n=22/24)	0
	32-63	pIRIR$_{290}$	0.99 ± 0.01 (n=23/24)	0
	180-250	IR$_{50}$ (PIRIR$_{180}$)	1.01 ± 0.04 (n=3/3)	0
	180-250	IR$_{50}$ (PIRIR$_{225}$)	0.96 ± 0.02 (n=3/3)	0
	180-250	IR$_{50}$ (PIRIR$_{290}$)	1.00 ± 0.02 (n=3/3)	0
	180-250	pIRIR$_{180}$	1.00 ± 0.02 (n=3/3)	0
	180-250	pIRIR$_{225}$	1.03 ± 0.03 (n=3/3)	0
	180-250	pIRIR$_{290}$	1.01 ± 0.03 (n=3/3)	0
Rock 7	32-63	IR$_{50}$	1.02 ± 0.01 (n=23/24)	2 ± 2
	32-63	pIRIR$_{290}$	1.02 ± 0.01 (n=24/24)	0
	180-250	IR$_{50}$ (PIRIR$_{180}$)	1.00 ± 0.02 (n=3/3)	0
	180-250	IR$_{50}$ (PIRIR$_{225}$)	1.02 ± 0.03 (n=3/3)	0
	180-250	IR$_{50}$ (PIRIR$_{290}$)	1.00 ± 0.02 (n=3/3)	0
	180-250	pIRIR$_{180}$	1.12 ± 0.14 (n=2/3)	13 ± 12
	180-250	pIRIR$_{225}$	1.02 ± 0.06 (n=3/3)	0
	180-250	pIRIR$_{290}$	1.00 ± 0.05 (n=2/3)	0
Rock 11	32-63	IR$_{50}$	1.01 ± 0.02 (n=20/24)	0
	32-63	pIRIR$_{290}$	1.02 ± 0.02 (n=20/24)	5 ± 3
	180-250	IR$_{50}$ (PIRIR$_{180}$)	1.03 ± 0.02 (n=3/3)	0
	180-250	IR$_{50}$ (PIRIR$_{225}$)	0.98 ± 0.02 (n=3/3)	0
	180-250	IR$_{50}$ (PIRIR$_{290}$)	0.96 ± 0.03 (n=3/3)	0
	180-250	pIRIR$_{180}$	1.12 ± 0.07 (n=3/3)	0
	180-250	pIRIR$_{225}$	1.02 ± 0.04 (n=2/3)	0
	180-250	pIRIR$_{290}$	0.98 ± 0.03 (n=3/3)	2 ± 6
Rock 12	32-63	IR$_{50}$	1.00 ± 0.02 (n=22/24)	3 ± 3
	32-63	pIRIR$_{290}$	0.99 ± 0.01 (n=21/24)	0
	180-250	IR$_{50}$ (PIRIR$_{180}$)	1.00 ± 0.02 (n=3/3)	0
	180-250	IR$_{50}$ (PIRIR$_{225}$)	1.00 ± 0.02 (n=3/3)	0
	180-250	IR$_{50}$ (PIRIR$_{290}$)	1.04 ± 0.02 (n=3/3)	0
	180-250	pIRIR$_{180}$	1.08 ± 0.04 (n=3/3)	0
	180-250	pIRIR$_{225}$	0.99 ± 0.03 (n=3/3)	0
	180-250	pIRIR$_{290}$	1.04 ± 0.03 (n=3/3)	0

Table S6, continued. Dose recovery test results for volcanic rocks used for dating at site CA21P1 in Cave Valley.

Rock sample	Grain size (µm)	Signal	Measured/given dose ratio	Sigma-b (%)
Rock 13	32-63	IR_{50}	1.02 ± 0.02 (n=19/24)	5 ± 3
	32-63	$pIRIR_{290}$	1.03 ± 0.02 (n=24/24)	3 ± 3
	180-250	IR_{50} ($PIRIR_{180}$)	0.99 ± 0.02 (n=3/3)	0
	180-250	IR_{50} ($PIRIR_{225}$)	1.00 ± 0.03 (n=3/3)	0
	180-250	IR_{50} ($PIRIR_{290}$)	1.01 ± 0.04 (n=3/3)	0
	180-250	$pIRIR_{180}$	1.03 ± 0.05 (n=3/3)	0
	180-250	$pIRIR_{225}$	0.97 ± 0.04 (n=3/3)	0
	180-250	$pIRIR_{290}$	1.09 ± 0.04 (n=3/3)	0
Rock 18	32-63	IR_{50}	1.03 ± 0.05 (n=14/24)	12 ± 4
	32-63	$pIRIR_{290}$	1.02 ± 0.04 (n=14/24)	6 ± 5
	180-250	IR_{50} ($PIRIR_{180}$)	1.01 ± 0.02 (n=3/3)	0
	180-250	IR_{50} ($PIRIR_{225}$)	1.01 ± 0.02 (n=3/3)	0
	180-250	IR_{50} ($PIRIR_{290}$)	1.05 ± 0.02 (n=3/3)	0
	180-250	$pIRIR_{180}$	1.15 ± 0.04 (n=3/3)	0
	180-250	$pIRIR_{225}$	1.01 ± 0.03 (n=3/3)	0
	180-250	$pIRIR_{290}$	1.04 ± 0.03 (n=3/3)	0

S6. Fading measurements and corrections

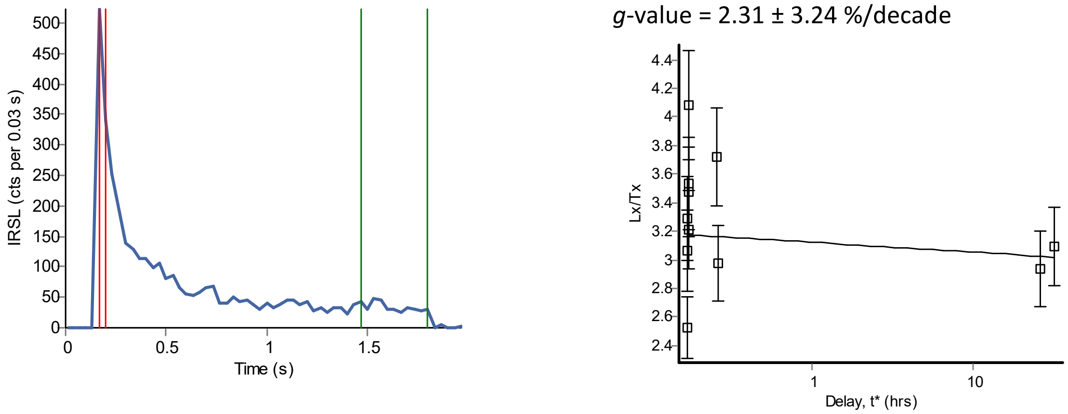
A) Rock 2 (63-90 µm)

B) Rock 2 (63-90 µm)
g-value = 2.31 ± 3.24 %/decade

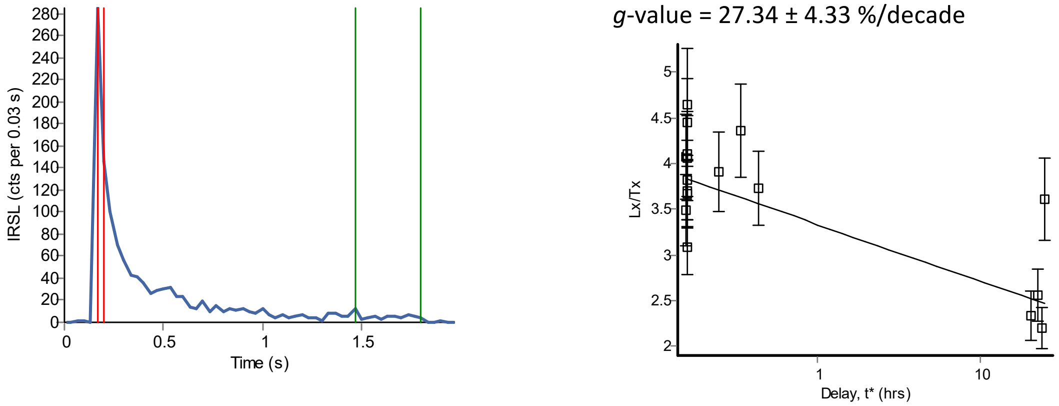
C) Rock 10 (125-180 µm)

D) Rock 10 (125-180 µm)
g-value = 27.34 ± 4.33 %/decade

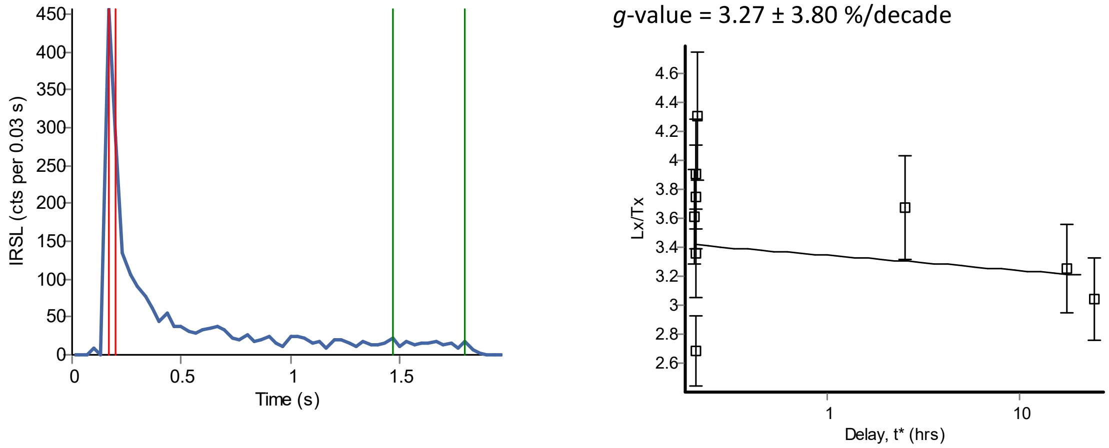
E) Rock 18 (180-250 µm)

F) Rock 18 (180-250 µm)
g-value = 3.27 ± 3.80 %/decade

Figure S12. Coal Valley CV21P1 sample IR_{50} signals from a single grain from each rock (left) and fading measurement results from the same grain (right). Signal fading approximates a log-linear rate.

A) Rock 2 (63-90 µm), n=64

B) Rock 2 (63-90 µm), n=59

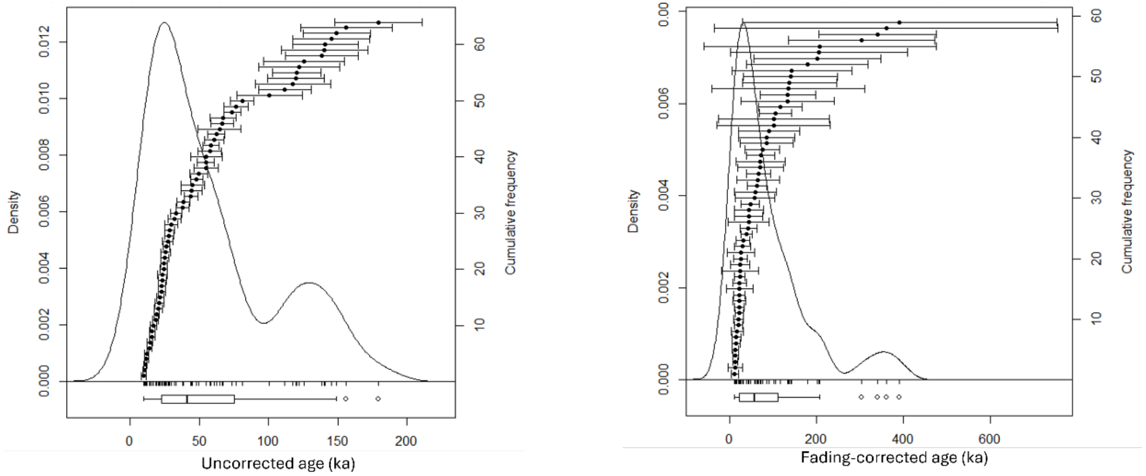

C) Rock 10 (125-180 µm), n=28

D) Rock 10 (125-180 µm), n=22

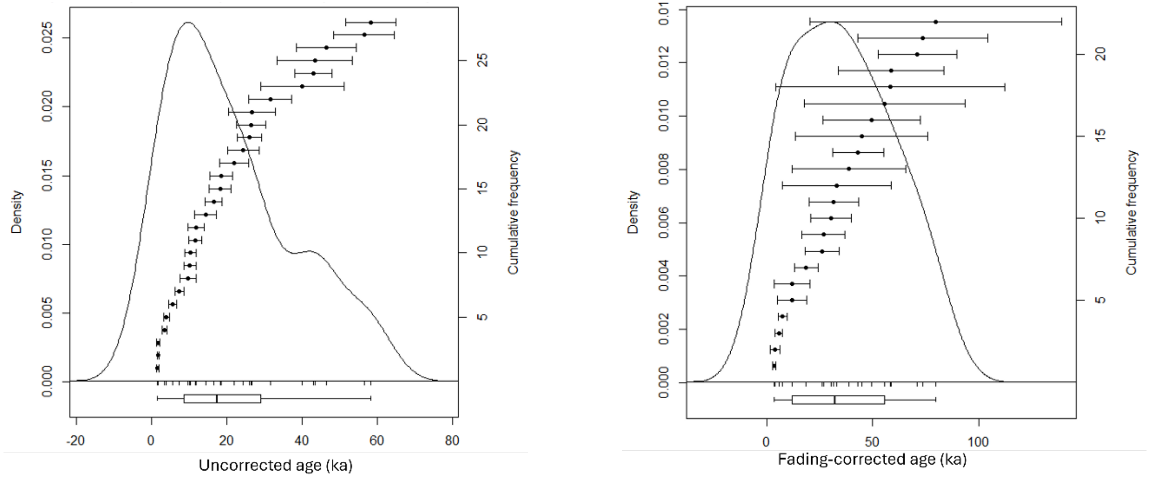

E) Rock 18 (180-250 µm), n=27

F) Rock 18 (180-250 µm), n=25

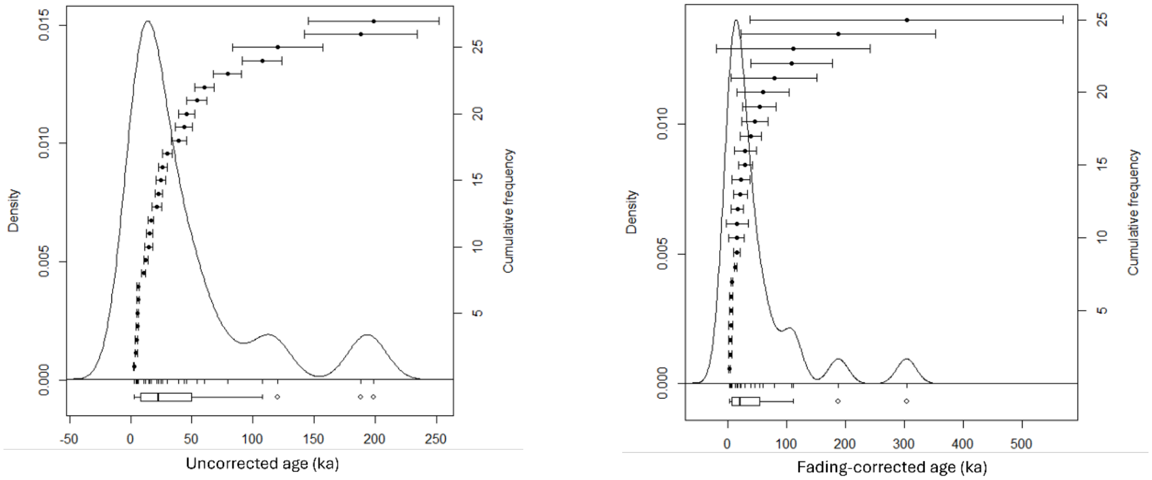

Figure S13. Uncorrected (left) and fading-corrected (right) aliquot age distributions for limestone Rocks 2, 10 and 18 from CV21P1 in Coal Valley. The cumulative distribution plot is superimposed on a kernel density estimate (KDE) curve. All grains were corrected for their own fading rate using the model of Huntley and Lamothe (2001). Grains with fading rates >10%/decade were rejected from analysis before fading correction.

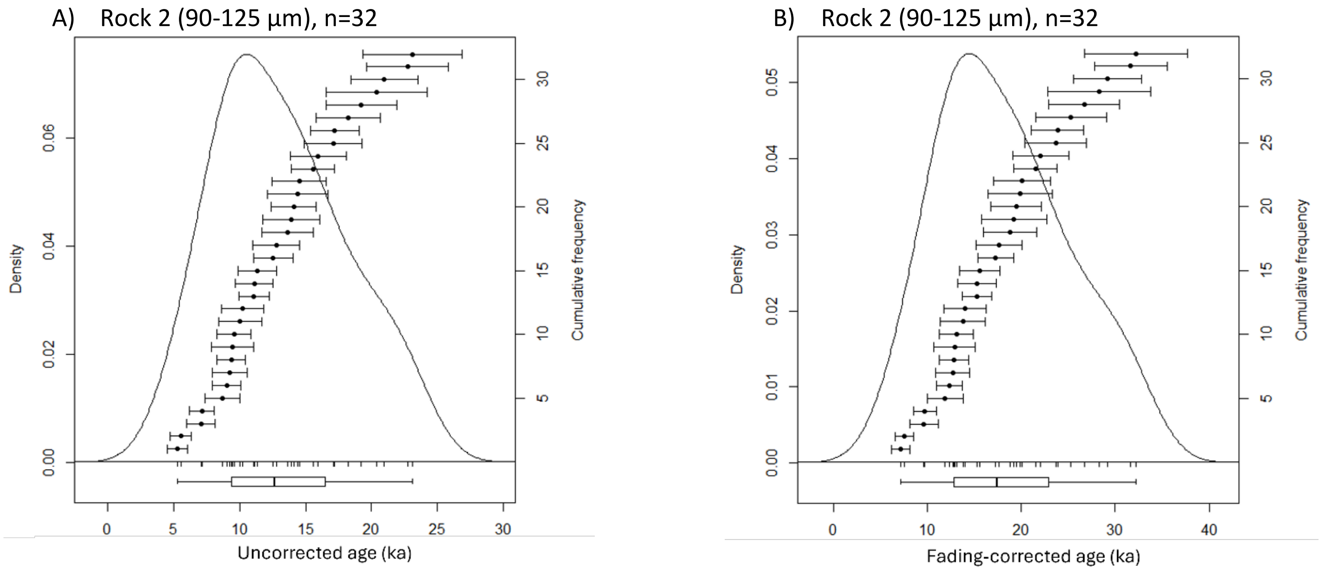

Figure S14. The uncorrected (A) and fading-corrected (B) age distribution for the 90-125 µm grain size fraction from Rock 2 of CV21P1. All aliquots were corrected using an average fading rate of 3.19 ± 0.15 %/decade measured from four 2 mm diameter aliquots.

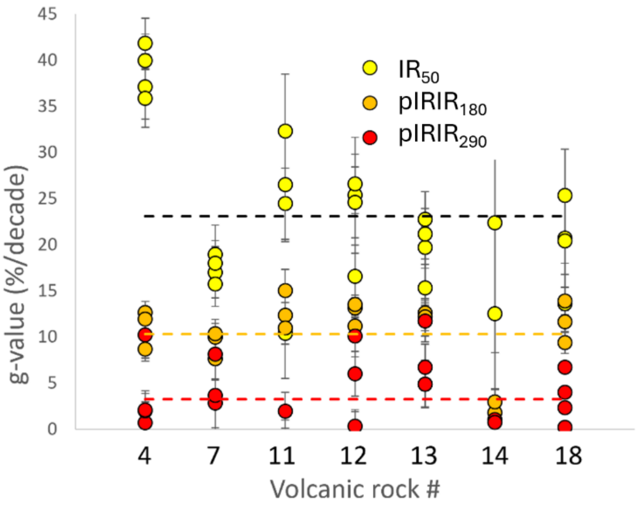

Figure S15. Measured fading rates for volcanic rocks collected from site CA21P1 in Cave Valley. Each dot represents one 3 mm diameter multi-grain aliquot. Black, yellow and red dashed lines mark the weighted mean *g*-values for the IR_{50}, $pIRIR_{180}$ and $pIRIR_{290}$ signals, respectively. The $pIRIR_{290}$ signal yielded an average *g*-value of 3.3 ± 0.7 %/decade, while the $pIRIR_{180}$ and IR_{50} signals yielded average *g*-values of 10.3 ± 0.9 and 23.1 ± 1.8 %/decade, respectively.

Table S7. Fading rates used for fading correction of volcanic rocks from site CA21P1 in Cave Valley. The *g*-value is the weighted mean fading rate calculated from four multi-grain aliquots measured for each rock.

Volcanic rock #	$pIRIR_{290}$ *g*-value (%/decade)
4	3.7 ± 2.2
7	3.5 ± 1.8
11	-0.7 ± 1.7
12	3.9 ± 1.3
13	6.6 ± 1.5
18	3.4 ± 1.3

S7. Radionuclide concentrations

Table S8. Radionuclide concentrations for limestone gravels sampled from site CV21P1 as determined by ICP-MS/AES and HPGe measurements.

Rock sample	Method	U nat (ppm)	Th (ppm)	K (%)	Rb (ppm)
Rock 2	ICP-MS/AES	0.57 ± 0.06	0.77 ± 0.08	0.23 ± 0.03	7.10 ± 0.71
Rock 10	ICP-MS/AES	1.00 ± 0.10	0.19 ± 0.02	0.02 ± 0.01	1.40 ± 0.14
Rock 18	ICP-MS/AES	0.51 ± 0.08	0.72 ± 0.09	0.17 ± 0.02	0.60 ± 0.06
Gravel matrix	ICP-MS/AES	1.61 ± 0.16	2.63 ± 0.26	0.52 ± 0.07	22.5 ± 2.25
Gravel matrix	HPGe	2.12 ± 0.06	0.54 ± 0.01	0.11 ± 0.01	--
Limestones (bulk)	HPGe	0.99 ± 0.14	0.78 ± 0.04	0.14 ± 0.01	--

Table S9. HPGe measurement of homogenized beach ridge sand from Skagen, Denmark (standard #063002).

	Specific activity (Bq/kg)			
	U-238	Th-232	Ra-226	K-40
This study	4.6 ± 0.5	4.5 ± 0.1	4.7 ± 0.1	334 ± 5
Murray et al., 2015	5.0 ± 0.3	3.9 ± 0.5	4.5 ± 0.4	333 ± 10

Table S10. CV21P1 sample radionuclide activity (Bq/kg) ratios for U and Th series determined using HPGe detection.

Sample	Ra-226 vs U-238	Pb-210 vs U-238	Pb-210 vs Ra-226	Ra-224 vs Ac-228
Gravel matrix	1.04 ± 0.03	1.28 ± 0.06	1.23 ± 0.05	0.80 ± 0.08
Limestones	0.93 ± 0.13	1.01 ± 0.30	1.08 ± 0.29	1.02 ± 0.20

Table S11. Volcanic gravel radionuclide contents of CA21P1 samples.

Rock sample	Method	U nat (ppm)	Th (ppm)	K (%)	Rb (ppm)
Rock 4	ICP-MS/AES	5.24 ± 0.52	18.6 ± 1.86	2.85 ± 0.28	139 ± 13.9
Rock 7	ICP-MS/AES	5.14 ± 0.51	21.4 ± 2.14	3.93 ± 0.39	181 ± 18.1
Rock 11	ICP-MS/AES	6.53 ± 0.65	22.5 ± 2.25	3.82 ± 0.38	169 ± 16.9
Rock 12	ICP-MS/AES	5.24 ± 0.52	18.9 ± 1.89	3.73 ± 0.37	171 ± 17.1
Rock 13	ICP-MS/AES	6.70 ± 0.67	21.0 ± 2.10	3.78 ± 0.38	189 ± 18.9
Rock 18	ICP-MS/AES	5.91 ± 0.59	20.6 ± 2.06	3.87 ± 0.39	166 ± 16.6
Gravel matrix	ICP-MS/AES	3.16 ± 0.32	10.9 ± 1.30	2.32 ± 0.23	98.1 ± 9.81
Gravel matrix	HPGe	3.27 ± 0.10	13.4 ± 0.07	2.42 ± 0.23	--

Table S12. Radionuclide activity ratios for the U and Th series determined using HPGe detection for gravel matrix from site CA21P1.

Sample	Ra-226 vs U-238	Pb-210 vs U-238	Pb-210 vs Ra-226	Ra-224 vs Ac-228
Gravel matrix	1.18 ± 0.04	1.39 ± 0.07	1.17 ± 0.04	0.99 ± 0.01

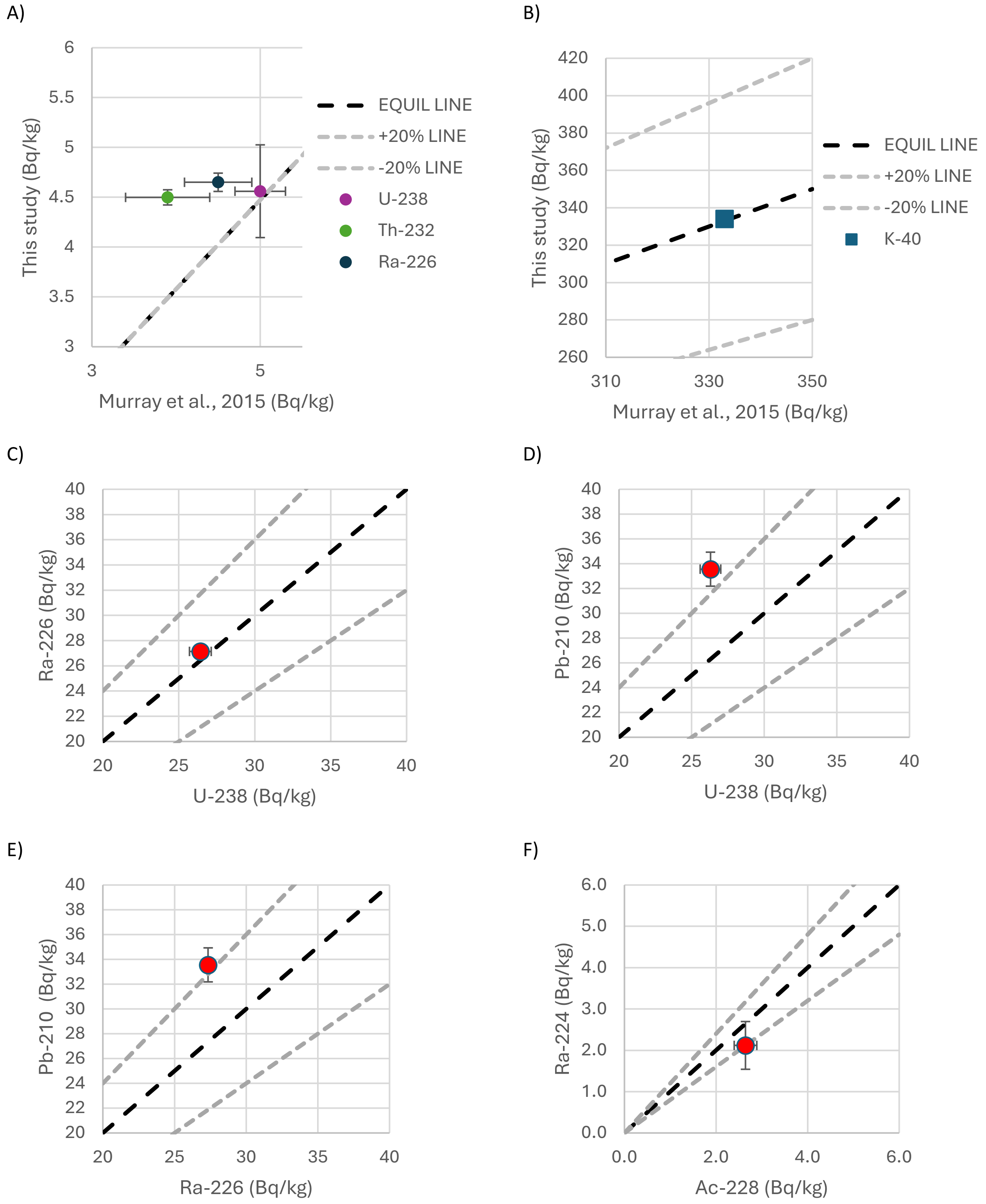

Figure S16. HPGe measurements of calibration standard Skagen 063002 (A & B). Measurements in this study are compared to those of Murray et al. (2015), which report the mean results from 23 laboratories. Our results are within 20% of those previously published. Error bars for K-40 are smaller than the size of the symbol. (C-F) Radionuclide activity ratios for the gravel matrix sample from site CV21P1. Grey dashed lines delineate ±20% of unity.

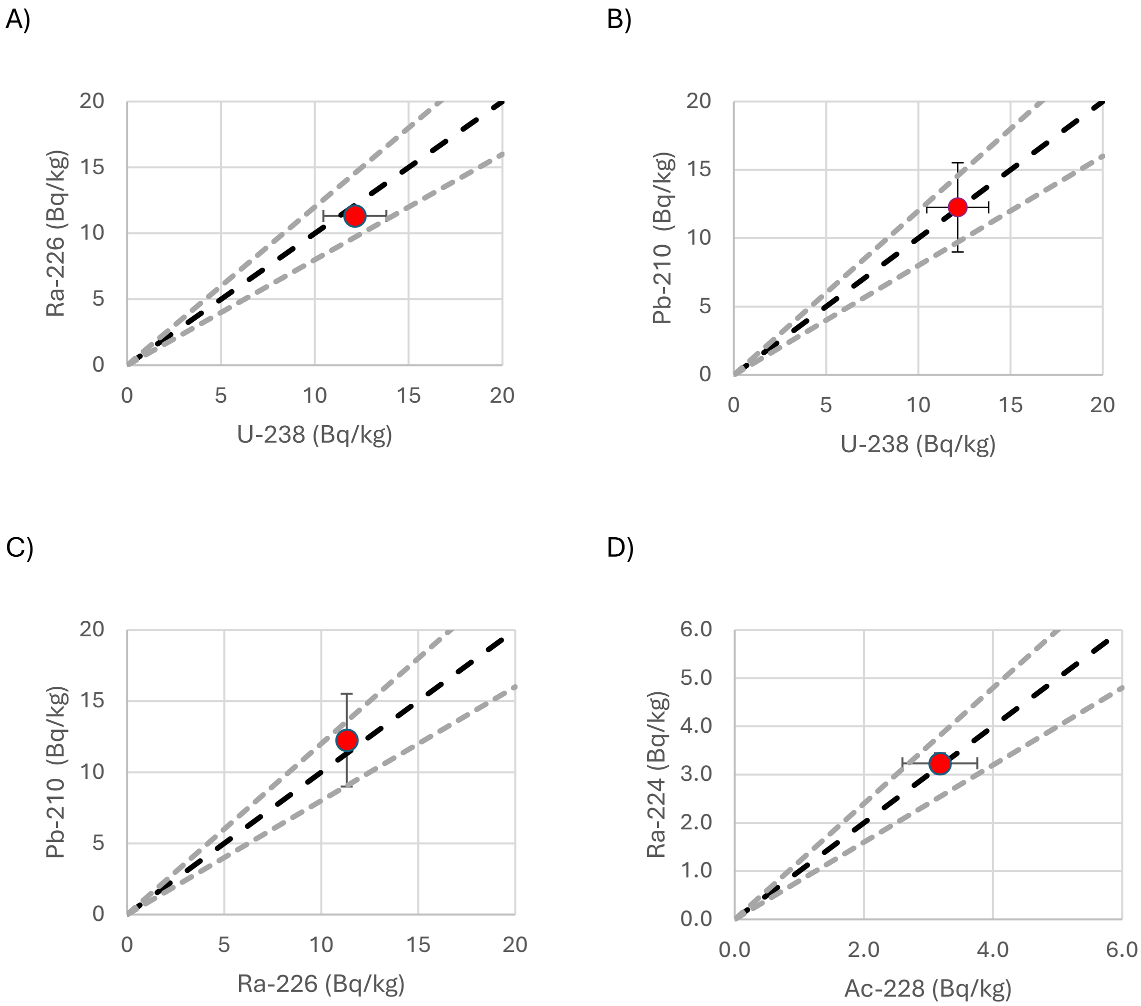

Figure S17. Radionuclide activity ratios for the limestone sample from site CV21P1. Grey dashed lines delineate ±20% of unity.

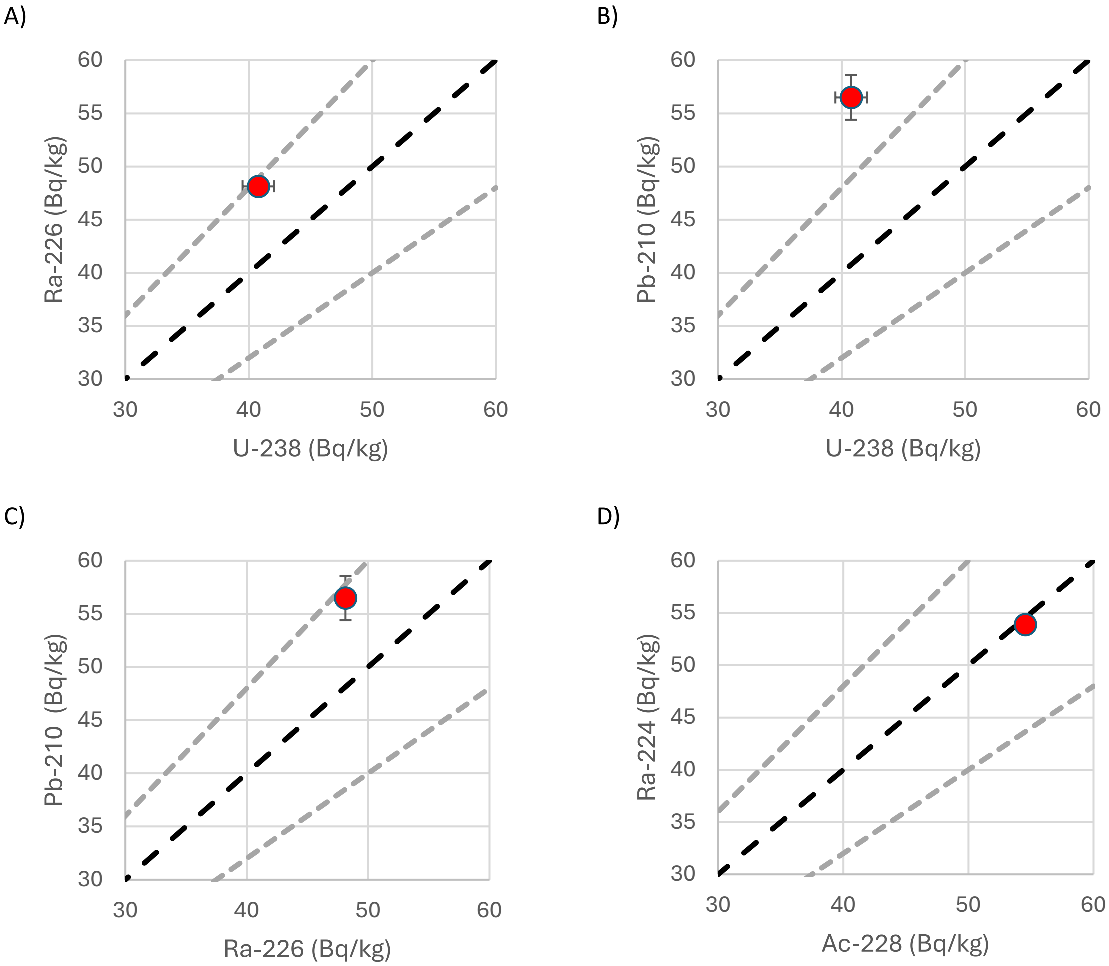

Figure S18. Radionuclide activity ratios for the U and Th series determined using HPGe detection for gravel matrix from site CA21P1.

S8. Dose rate modeling for rocks

Dose rate with depth models for limestone rocks were calculated using the method of Jenkins et al. (2018) and Riedesel and Autzen (2020) for comparison (Fig. S19); only the Riedesel and Autzen (2020) model is used for final age calculations in the main text and in Tables S13 and S14. The method of Jenkins et al. uses the approach of Aitken (1985, Appendix H) and Freiesleben et al. (2015) where the beta dose with depth (x) into a rock is calculated as:

$$\dot{D}(x)_{\beta}^{Rock} = \dot{D}_{Rock,\beta}^{inf}\left[1 - 0.5\left(e^{-bx} + e^{-b(h-x)}\right)\right] + \dot{D}_{Sed,\beta}^{inf}0.5\left(e^{-bx} + e^{-b(h-x)}\right) \qquad \text{(S1)}$$

Here, *b* is the beta attenuation factor (1.9 mm^{-1}) following Sohbati et al. (2015) and $\dot{D}_{Rock,\beta}^{inf}$ and $\dot{D}_{Sed,\beta}^{inf}$ are the infinite matrix beta dose rates for the rock and sediment, respectively. The same equation is used to calculate the gamma dose rate with depth, ($\dot{D}(x)_{\gamma}^{Rock}$, and this uses a gamma attenuation factor of 0.02 mm^{-1}, which is density-corrected for an assumed rock density of 2.6 g/cm^{2}. The sediment alpha contribution is ignored, due to the short distances (~10 mm) travelled by alpha particles, and the alpha contribution arising from the gravel is calculated using an a-value of 0.15 ± 0.05 (Balescu and Lamothe, 1994). Calculated total dose rates of the more recent Reidesel and Autzen (2020) approach are lower than those of Jenkins et al. (2018) (Fig. S19).

Table S13. Calculated gravel and sediment dose rates for site CV21P1.

Rock sample	Grain size [1] (µm)	Method [2]	Alpha [3] (Gy/ka)	Beta [3] (Gy/ka)	Gamma [3] (Gy/ka)	Cosmic (Gy/ka)	Total [4] (Gy/ka)
Rock 2	90-125	ICP/AES	0.05 ± 0.01	0.28 ± 0.01	0.02 ± 0.01	0.25 ± 0.03	1.24 ± 0.09
Rock 2	63-90	ICP/AES	0.07 ± 0.02	0.28 ± 0.03	0.02 ± 0.01	0.25 ± 0.03	1.17 ± 0.07
Rock 10	125-180	ICP/AES	0.05 ± 0.02	0.14 ± 0.01	0.01 ± 0.01	0.24 ± 0.02	1.21 ± 0.12
Rock 18	180-250	ICP/AES	0.02 ± 0.01	0.20 ± 0.02	0.01 ± 0.01	0.25 ± 0.03	1.47 ± 0.17
Gravel matrix	125-180	ICP/AES	0.11 ± 0.03	0.64 ± 0.07	0.42 ± 0.04	0.25 ± 0.03	1.85 ± 0.14
Gravel matrix	125-180	HPGe	0.10 ± 0.04	0.35 ± 0.02	0.28 ± 0.02	0.25 ± 0.03	1.41 ± 0.13
Crushed limestone	125-180	HPGe	0.06 ± 0.02	0.25 ± 0.01	0.18 ± 0.02	0.25 ± 0.03	1.17 ± 0.12

[1] Dose rates for gravel matrices are reported here for the 125-180 µm grain size fraction only.

[2] Method of radionuclide measurement. ICP-MS (ICP) was used to measure U and Th contents, and ICP-AES (AES) was used to measure K contents by ALS Minerals, Reno, NV. HPGe measurements were used to obtain U, Th and K contents at DRILL.

[3] External alpha, beta and gamma dose rates have been corrected for grain size and water content. Alpha dose rates assume an a-value of 0.15 ± 0.05 following Balescu and Lamothe (1994).

[4] The total dose rate for the outer 2 mm of each rock has been calculated using the model of Riedesel and Autzen (2020) and includes an internal beta dose rate component that assumes an internal K content of 10 ± 2 % for feldspar grains following Smedley et al. (2012). Dose rates for gravel matrices and the crushed limestone sample are shown for comparison and have been calculated assuming a laterally infinite matrix using the Dose Rate and Age Calculator (DRAC) of Durcan et al. (2015).

Table S14. Calculated gravel and sediment dose rates for site CA21P1.

Rock sample	Grain size [1] (µm)	Method [2]	Alpha [3] (Gy/ka)	Beta [3] (Gy/ka)	Gamma [3] (Gy/ka)	Cosmic (Gy/ka)	Total [4] (Gy/ka)
Rock 4	32-63	ICP/AES	1.00 ± 0.22	3.12 ± 0.23	0.13 ± 0.01	0.31 ± 0.03	6.22 ± 0.33
Rock 7	32-63	ICP/AES	1.07 ± 0.23	4.34 ± 0.33	0.15 ± 0.01	0.30 ± 0.03	7.33 ± 0.42
Rock 11	32-63	ICP/AES	1.23 ± 0.27	4.08 ± 0.31	0.14 ± 0.01	0.32 ± 0.03	7.44 ± 0.42
Rock 12	32-63	ICP/AES	1.01 ± 0.22	3.78 ± 0.29	0.13 ± 0.01	0.31 ± 0.03	6.90 ± 0.38
Rock 13	32-63	ICP/AES	1.20 ± 0.26	4.04 ± 0.30	0.40 ± 0.02	0.31 ± 0.03	7.31 ± 0.41
Rock 18	32-63	ICP/AES	1.12 ± 0.24	4.01 ± 0.31	0.17 ± 0.01	0.31 ± 0.03	7.23 ± 0.41
Gravel matrix	32-63	ICP/AES	0.57 ± 0.13	2.47 ± 0.24	1.41 ± 0.12	0.30 ± 0.03	4.88 ± 0.25
Gravel matrix	32-63	HPGe	0.65 ± 0.14	2.61 ± 0.16	1.56 ± 0.09	0.30 ± 0.03	5.25 ± 0.16

[1] Dose rates for gravel matrices are reported here for the 32-63 µm grain size fraction only.

[2] Method of radionuclide measurement. ICP-MS (ICP) was used to measure U and Th contents, and ICP-AES (AES) was used to measure K contents by ALS Minerals, Reno, NV. HPGe measurements were used to obtain U, Th and K contents at DRILL.

[3] External alpha, beta and gamma dose rates have been corrected for grain size and water content. Alpha dose rates assume an a-value of 0.10 ± 0.05 for the 32-63 µm grain size fraction.

[4] The total dose rate for the outer 1 mm of each rock has been calculated using the model of Riedesel and Autzen (2020) and includes an internal beta dose rate component that assumes an internal K content of 10 ± 2 % for feldspars following Smedley et al. (2012). Dose rates for gravel matrices are shown for comparison and have been calculated assuming a laterally infinite matrix using the Dose Rate and Age Calculator (DRAC) of Durcan et al. (2015). Rock dose rates calculated for crushed rock slices (Sections 4.4.6 & 4.4.8) are adjusted to the sieved grain size fraction (125 to 250 µm) used for rock slice D_e measurements as well as dose rate attenuation with depth into the rock.

A) Rock 2 (63-90 µm), Jenkins et al. (2018)

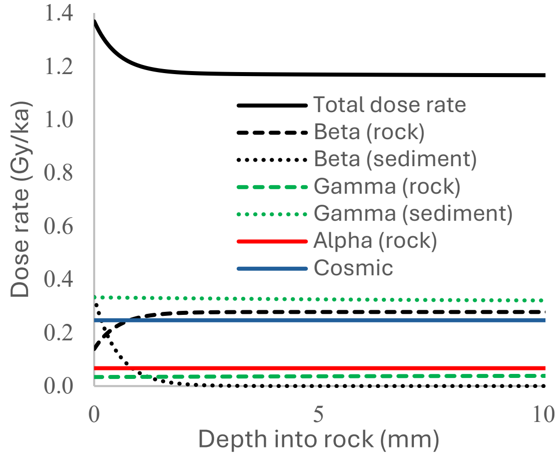

B) Rock 2 (63-90 µm), Riedesel & Autzen (2020)

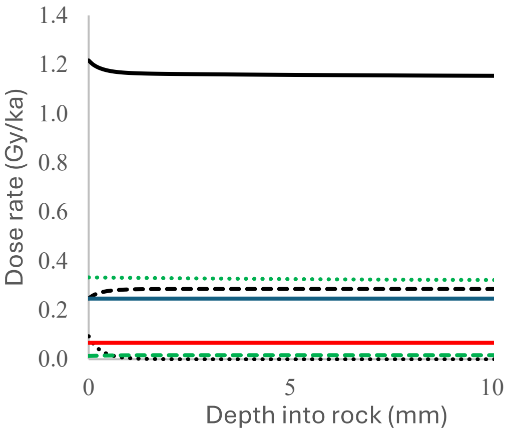

C) Rock 2 (90-125 µm), Jenkins et al. (2018)

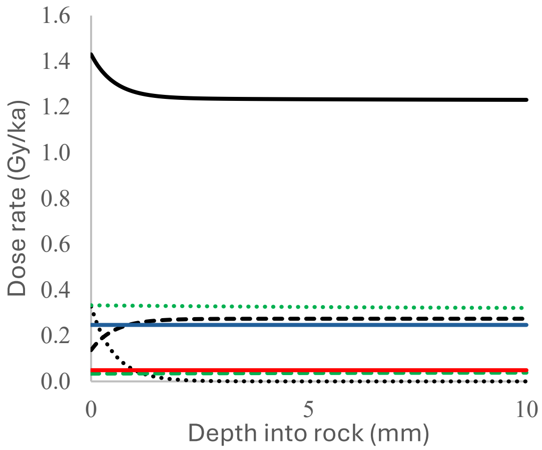

D) Rock 2 (90-125 µm), Riedesel & Autzen (2020)

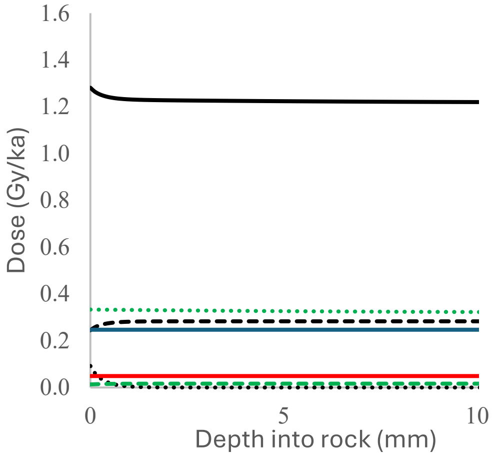

E) Rock 10 (125-180 µm), Jenkins et al. (2018)

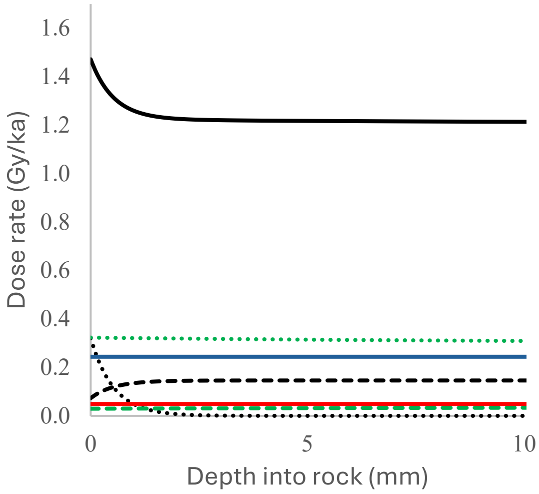

F) Rock 10 (125-180 µm), Riedesel & Autzen (2020)

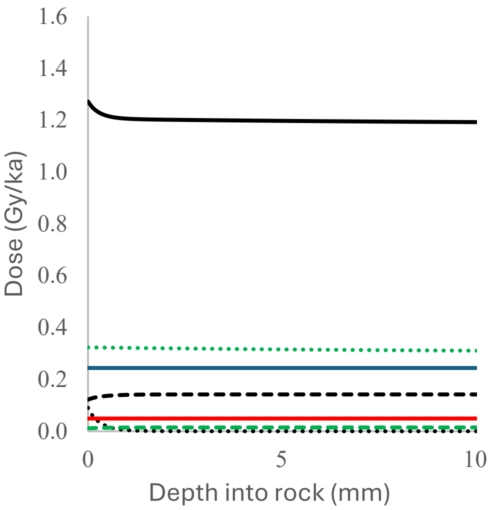

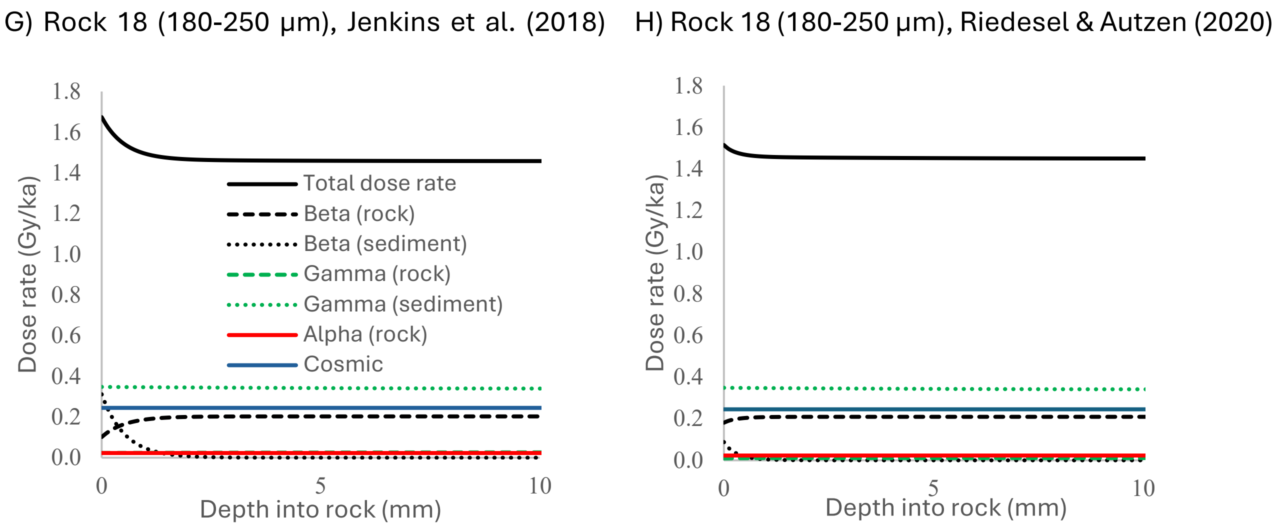
G) Rock 18 (180-250 µm), Jenkins et al. (2018)

H) Rock 18 (180-250 µm), Riedesel & Autzen (2020)

Figure S19. A comparison of two dose rate with depth models for limestone rocks from CV21P1. Total dose rates include an internal dose rate based on an assumed internal K content of 10 ± 2% for feldspar grains following Smedley et al. (2012).

S9. Statistical models for calculating sample D_e and their assumptions

Central Dose Model

The central dose model (CDM or CAM) assumes that the sample has been completely re-set by sunlight prior to burial (Galbraith et al.,1999). The CAM estimates a "geometric weighted mean" from logged D_e distributions (i.e., the x-axis of the Kernel density estimate distribution is logged). The D_e distributions are logged prior to mean calculation, because D_e values tend to correlate positively with D_e errors (adding to positive skewness in the unlogged D_e distribution), so CAM is an attempt to avoid age over-estimations resulting from this positive skew.

Minimum Dose Model

The minimum dose model (MDM or MAM), is applied to samples thought to have been partially bleached leading to a truncated log-normal D_e distribution with a positive skew (Galbraith et al.,1999). The MAM calculates a D_e estimate from the lower (younger) limb of the distribution to estimate the most recent bleaching event.

Average Dose Model

The average dose model, or ADM, is applied to samples that: i) are thought to be fully bleached prior to burial, and ii) are affected by a heterogeneous dose rate environment at the grain-scale (Guérin et al., 2017). These heterogeneities are typically associated with "hot" spots generated by K-rich feldspar grains. Modeling suggests that hotspots should lead to positively skewed D_e distributions (Mayya et al., 2006). On a positively skewed D_e distribution, the calculated ADM D_e value will always be higher than the CAM D_e value.

The authors of the ADM model argue that an age should be calculated using an *average* D_e value, rather than a *geometric* mean D_e value (like CAM) because we divide our sample D_e value by an *average* dose rate (measured by ICP-MS or gamma spectrometry, for example) to obtain an age. Due to the limits of our technology, we cannot measure the *single-grain dose rate* distribution—just an *average dose rate* for the sample. Therefore, they believe that the traditional method of dividing a geometric weighted mean D_e value (CAM) by an average dose rate will lead to an age underestimate.

S10. D_e-depth profiles from volcanic rocks

A) Rock 4

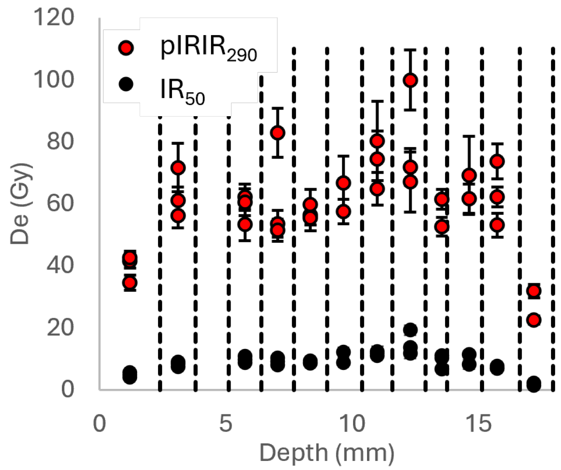

B) Rock 7 Core 1

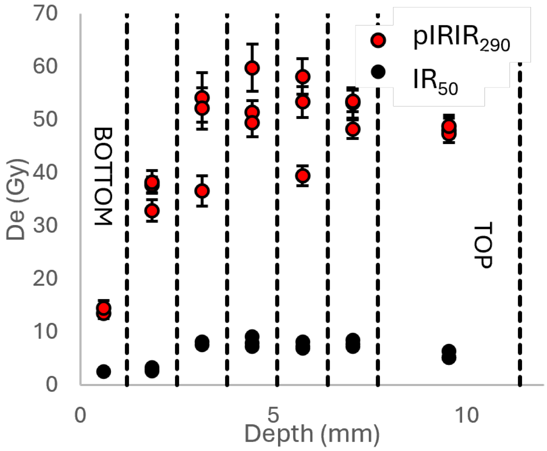

C) Rock 7 Core 2

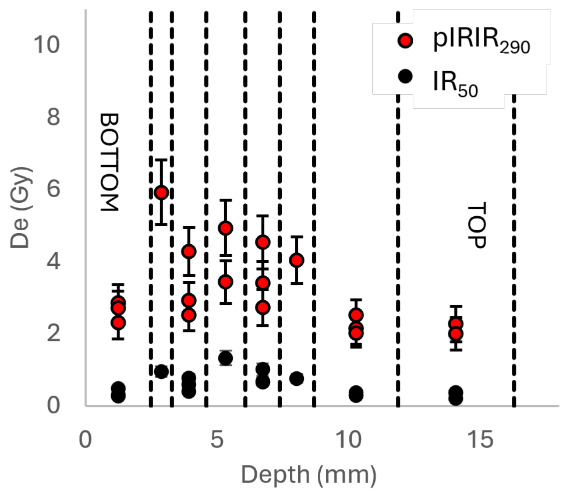

D) Rock 11

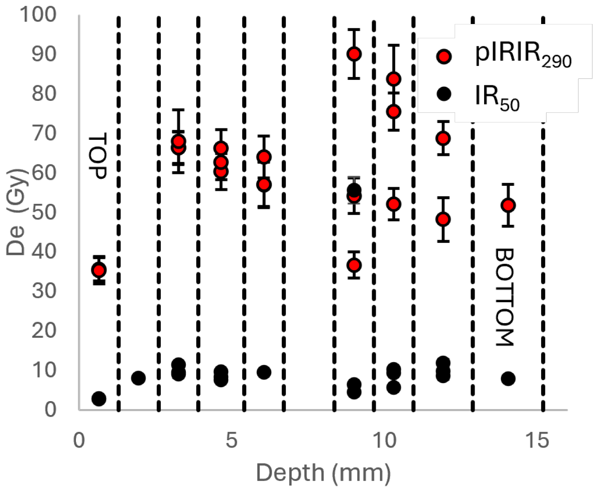

E) Rock 13

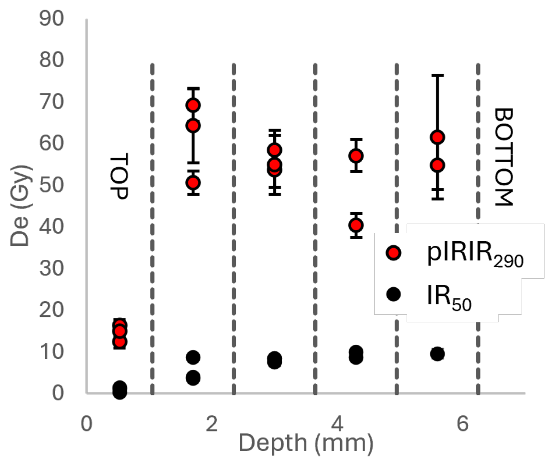

Figure S20. Rock D_e plotted with depth for cores extracted from Rocks 4, 7, 11 and 13 from CA21P1 in Cave Valley. Dashed lines denote slice boundaries. Aliquots contain ~125 grains each of the 125-250 µm fraction. Top and bottom of the rock indicated for oriented samples.

A) Rock 18 Core 1

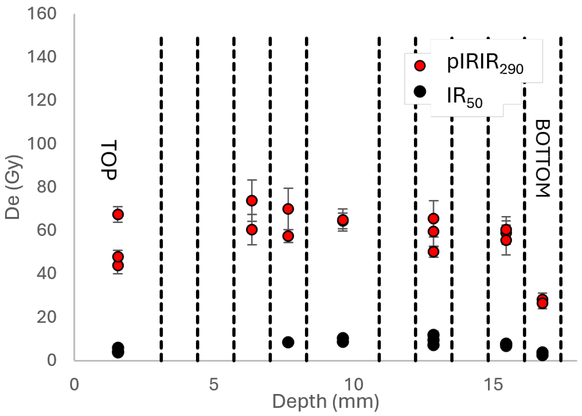

B) Rock 18 Core 2

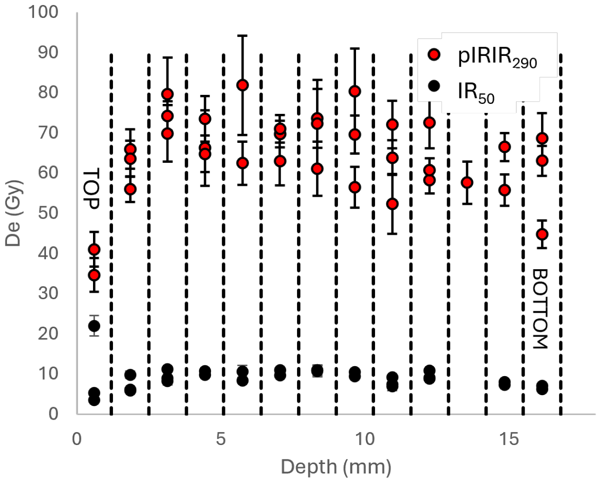

C) Rock 18 Core 3

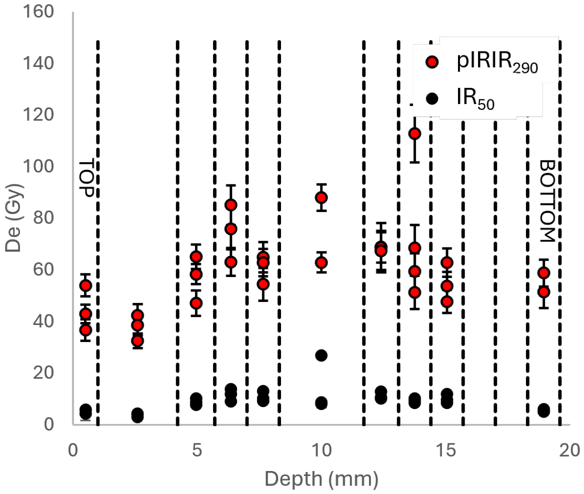

Figure S21. D_e plotted with depth for 3 cores extracted from Rock 18 from CA21P1 in Cave Valley. Dashed lines denote slice thickness. Aliquots contain ~125 grains each of the 125-250 µm fraction. Top and bottom of the rock indicated for oriented samples.

References

Aitken, JM (1985) Thermoluminescence Dating. Academic Press, London.

Balescu, S, Lamothe, M (1994) Comparison of TL and IRSL age estimates of feldspar coarse grains from waterlain sediments. Quaternary Science Reviews 13(5-7): 437–444.

Bulur, E (1996) An alternative technique for optically stimulated luminescence (OSL) experiment. Radiation Measurements 26: 701–709.

Crafford, AEJ (2007) Geologic Map of Nevada: U.S. Geological Survey Data Series 249, 1 CD-ROM, 46 p., 1 plate.

Dietze, M (2021) plot_KDE(): Plot kernel density estimate with statistics. Function version 3.6.0. In: Kreutzer, S, et al. (2021) Luminescence: Comprehensive Luminescence Dating Data Analysis. R package version 0.9.14. https://CRAN.R-project.org/package=Luminescence

Dietze, M, Kreutzer, S (2021) plot_AbanicoPlot(): Function to create an Abanico Plot.. Function version 0.1.15. In: Kreutzer, S et al. (2021) Luminescence: Comprehensive Luminescence Dating Data Analysis. R package version 0.9.14. https://CRAN.R-project.org/package=Luminescence

Duke, D., Young, D. C. (2018) A historic context for Paleoamerican archaeology. Bureau of Land Management Report No.: 8111 CRR NV 040-15-2113, Lincoln County Archaeological Initiative, Round 7.

Freiesleben, T, Sohbati, R, Murray, A, Jain, M, Khasawneh, S, Hvidt, S, Jakobsen, B (2015) Mathematical model quantifies multiple daylight exposure and burial events for rock surfaces using luminescence dating. Radiation Measurements 81: 16–22.

Galbraith, RF, Roberts, RG, Laslett, GM, Yoshida, H, Olley, JM (1999) Optical dating of single and multiple grains of quartz from Jinmium rock shelter, northern Australia: Part I, experimental design and statistical models. Archaeometry 41: 339–364.

Guérin, G, Christophe, C, Philippe, A, Murray, AS, Thomsen, KJ, Tribolo, C, Urbanova, P, Jain, M, Guibert, P, Mercier, N, Kreutzer, S, and Lahaye, C (2017) Absorbed dose, equivalent dose, measured dose rates, and implications for OSL age estimates: Introducing the Average Dose Model. Quaternary Geochronology 41: 163–173.

Huntley, DJ, Lamothe, M (2001) Ubiquity in anomalous fading in K-feldspars and the measurement and correction for it in optical dating. Canadian Journal of Earth Science 38: 1093–1106.

Jenkins, GTH, Duller, GAT, Roberts, HM, Chiverrell, RC, Glasser, NF (2018) A new approach for luminescence dating glaciofluvial deposits – High precision optical dating of cobbles. Quaternary Science Reviews 192: 263–273.

Lillquist, K. D. (1994) Late Quaternary Lake Franklin: Lacustrine chronology, coastal geomorphology, and hydro-isostatic deflection in Ruby Valley and northern Butte Valley, Nevada. PhD Thesis, Department of Geography, University of Utah. 185 p.

Mayya, YS, Morthekai, P, Murari, MK, Singhvi, AK (2006) Towards quantifying beta microdosimetric effects in single-grain quartz dose distribution. Radiation Measurements 41: 1032–1039.

Murray, A, Buylaert, J-P, Thiel, C (2015) A luminescence dating intercomparison based on a Danish beach-ridge sand. Radiation Measurements 81: 32–38.

Reimer et al. (2020) The IntCal20 Northern Hemisphere Radiocarbon Age Calibration Curve (0-55 cal kBP). Radiocarbon 62(4): 725–757.

Riedesel, S, Autzen, M (2020) Beta and gamma dose rate attenuation in rocks and sediment. Radiation Measurements 133: 106295.

Roberts, HM (2007) Assessing the effectiveness of the double-SAR protocol in isolating a luminescence signal dominated by quartz. Radiation Measurements 42: 1627–1636.

Smedley, RK, Duller, GAT, Pearce, NJG, and Roberts, HM (2012) Determining the K-content of single-grains of feldspar for luminescence dating. Radiation Measurements 47: 790–796.

Wriston, T., Adams, K. D. (2020) LCAI Coal Valley Archaeological and Geomorphological Research: Pluvial Lake Coal and Paleoindians. BLM Report No. 8111 NV-04-17-2170 on file at the BLM, Ely District Office.